Photon Rings and Shadow Size for General Integrable Spacetimes

by

Kiana Salehi

A thesis
presented to the University of Waterloo
in fulfillment of the
thesis requirement for the degree of
Master of Science
in
Physics

Waterloo, Ontario, Canada, 2023

Author's Declaration

This thesis consists of material all of which I authored or co-authored: see Statement of Contributions included in the thesis. This is a true copy of the thesis, including any required final revisions, as accepted by my examiners.

I understand that my thesis may be made electronically available to the public.

Statement of Contribution

This thesis incorporates content from two papers that are currently being prepared for publication. It is important to acknowledge that the content in chapters 2 and 3 has been developed in collaboration with the individuals listed below.:

Prof. Avery Broderick

Department of Physics and Astronomy, University of Waterloo

Waterloo Centre for Astrophysics, University of Waterloo

Perimeter Institute for Theoretical Physics

Boris Georgiev

Department of Physics and Astronomy, University of Waterloo

Waterloo Centre for Astrophysics, University of Waterloo

Perimeter Institute for Theoretical Physics

Abstract

According to the no-hair theorem, the unique characteristics of astrophysical black holes are their masses and spins. However, recent observations from the Event Horizon Telescope (EHT) images of M87 and Sgr A* have allowed us to place constraints on possible deviations from this theory. To interpret these observations and compare them to other near horizon scale observations, we introduce a model-agnostic framework that explores deviations while maintaining generality. We start by considering a general spherically symmetric metric, which effectively applies for a polar observer in the slow rotation limit and then follow by relaxing these constraints to axi-symmetric and stationary spacetimes. We propose a nonperturbative, nonparametric spacetime-domain characterization of shadow size and related measurements that makes explicit the nature and power (or lack thereof) of shadow-size-based constraints, and facilitates comparisons among observations and targets. Furthermore, we demonstrate that relying solely on shadow size measurements does not impose a direct limitations on the value of the g_{tt} component of the metric. However, in the case of spherically symmetric spacetime, it can impose a constraint on the radial derivative of g_{tt}, while a more intricate constraint arises for the axi-symmetric spacetime. Moreover, the measurement of shadows and potential future observations of multiple photon rings do not provide any valuable information concerning the ergo-region and frame-dragging in axi-symmetric spacetime.

Acknowledgements

I express my utmost gratitude to my supervisor, Prof. Avery Broderick, for his constant and priceless guidance and support throughout my research. I would like to express my appreciation to Dr. Broderick's group, particularly Boris Georgiev, for the valuable discussions we had and their assistance. Additionally, I would like to thank Prof. Niayesh Afshordi and Dr. Luis Lehner for agreeing to be part of my committee and for engaging in meaningful discussions.

I also would like to thanks Taillte May, Sercan Husnugil, Ramiro Cayuso and Saba Etezad Razavi for the valuable discussion and support. Also my dear family for all of their support.

Table of Contents

List of Figures

List of Tables

Chapter 1

Introduction

Until approximately a century ago, scientists relied on Newton's law of universal gravitation to explain the properties of gravity. However, in 1915, Einstein revolutionized this field by introducing the general theory of relativity, which remains the prevailing model of gravitation in modern physics [29].

The purely geometrical perspective of spacetime, has created extensive opportunities for physicists to describe a wide range of phenomena, from the solar system to the vast structure of the cosmos. Since this thesis centers around testing theories in the strong gravity regime, where general relativity is crucial, I will offer a concise summary of GR followed by a brief overview of recent measurements by the Event Horizon Telescope and alternative theories that aim to describe gravity.

1.1 General Relativity

One of the fundamental concept in general relativity is the geodesic motion [85]. This concept is particularly significant in understanding the behavior of light and matter in the presence of massive objects such as stars and black holes. Since we are going to assume photons continue to follow the null geodesics in the following chapters , we review this concept here. A **geodesic** is defined as,

$$P^{\alpha}\nabla_{\alpha}P^{\mu} = dP^{\mu}/d\lambda + \Gamma^{\mu}_{\sigma\beta}P^{\sigma}P^{\beta} = 0, \tag{1.1}$$

where Γ is the Christofell symbol, P^{α} is the particle's momentum's 4-vector and λ is the affine parameter.

Moreover, in the context of general relativity, massive objects curve the surrounding spacetime. The curvature follows the Einstein field equation,

$$R_{\mu\nu} - \frac{1}{2} g_{\mu\nu} R = \kappa T_{\mu\nu}, \tag{1.2}$$

where $R_{\mu\nu}$ and R are respectively Ricci tensor and Ricci scalar, and κ is a constant that is a function of fundamental constants of nature, c and G. It is noteworthy to mention that alternative theories possess distinct field equations, resulting in diverse spacetime solutions for various scenarios, which we will briefly mention in Appendix I and Appendix J.

As a result, within GR geodesics no longer appear as straight lines, but are bent, a phenomena called gravitational lensing. The phenomenon has been observed numerous times ([51, 59, 80]) and has provided crucial evidence for the existence of massive objects such as black holes. The images of black holes that were captured using the Event Horizon Telescope depict the direct impact of this phenomenon which we are going to expand further later in the introduction [30, 31, 32, 33, 34, 35].

Extreme gravitational lensing is observed in the first horizon-resolving images of black holes at the centres of Messier 87 (M87*) and the Milky Way (Sgr A*)[30, 31, 32, 33, 34, 35, 36, 37, 40, 39, 41, 38]. Photons coming from the entire universe, but in the case of black holes mostly from the accretion disk, are deflected around the central massive object. The angle of deflection is tightly related to the impact parameter of the null ray. To provide an explanation of this phenomenon, we can begin with the most basic category of black holes in GR known as Schwarzschild black holes. Within this classification, there exists an unstable photon circular ring positioned at a distance of $r_\gamma = 3M$, where M represents a specific parameter associated with the black hole and in natural units i.e, $G = c = 1$ [1].

This circular orbit is a direct consequence of highly lensed null trajectories. Photons with a critical impact parameter, precisely equal to $b_\gamma = \sqrt{27M}$ get highly deflected around the black hole and circulate around it (for further details, refer to the Appendix A). The magnitude of this impact parameter determines the observed size of the shadow visible in images of the black hole [35, 41]. However, even a slight deviation in these null rays' impact parameters will result in significantly different trajectories.

Null rays that originate slightly outside of r_γ circulate around the black hole a finite amount of times, denoted as 'n', before escaping towards infinity. Each of these paths forms a ring around the black hole. To characterize the behavior of these subsequent rings, one can define the Lyapunov exponent as,

$$\pi \frac{d\delta r}{d\phi} = \gamma \delta r \tag{1.3}$$

[1] we are claiming everything in natural unit, unless otherwise is mentioned

Here, ϕ corresponds to the azimuthal angle within the plane where the orbit exists and δr is the distance between the subsequent null ray and r_γ. The value of Lyapunov exponent for Schwarzschild metric is equal to π (see Appendix B for more detail).

The case of spinning black holes is a bit more complex. Similar to the Schwarzschild spacetime, photons with a specific impact parameters give rise to a critical unstable circular orbit. However, in the context of Kerr spacetime, the impact parameters on the celestial sphere of a distant observer are more intricate compared to those in the Schwarzschild spacetime. Nevertheless, for the purposes of the upcoming chapters, we will focus on photon orbits observed by polar observers, simplifying the case. In this scenario, it can be demonstrated that the radius of the photon's circular orbit and the size of its shadow are given by,

$$\begin{aligned} r_\gamma &= M + 2M\sqrt{1-\frac{a^2}{3M}}\cos\left[\frac{1}{3}\cos^{-1}\left(\frac{1-a^2/M^2}{(1-a^2/3M)^{3/2}}\right)\right]. \\ \beta^2 &= \frac{(r_\gamma^2+a^2)^2}{\Delta(r_\gamma)} \end{aligned} \tag{1.4}$$

where:

$$\Delta = r^2 - 2Mr + a^2 \tag{1.5}$$

and a represents the spin of Kerr black hole. Equation 1.4 is compatible with the results we saw in the Schwarzschild spacetime in the slow rotating regime (see Appendix C and Appendix F for more detail). Additionally, the Lyapunov exponent related to the subsequent null rays encircling a Kerr black hole can be defined. Nonetheless, we choose to address this topic in section 3.4 when we are probing a general axi-symmetric and stationary spacetimes (also see Appendix D, for more details).

Hence, according to General Relativity, the observation of a black hole entails the anticipation of a dark region accompanied by a bright area formed by subsequent photons [14]. Nevertheless, while General Relativity stands as the widely accepted theory for gravity, it is not the only theory attempting to describe this phenomenon. We explore the spherically symmetric spacetimes briefly in subsection 2.2.2, subsection 2.2.3 and Appendix I and the axi-symmetric ones in subsection 3.5.2 and Appendix J.

1.2 Observational Tests of GR

Since the emergence of General Relativity a hundred years ago, various observations have been proposed to explore spacetime. However, only recently have a significant number of

these become possible. Since, the main aim of this thesis is to present a general formalism that enables the comparison of these tests, aiding our understanding of spacetime, in this subsection, we review some well-known observations that actively investigate the properties of gravity.

1.2.1 Event Horizon Telescope

The event horizon telescope (EHT) is a worldwide network of synchronized radio observatories that collaborate to observe radio sources associated with supermassive objects that are possible candidates of black holes. Using data from numerous telescopes that use the very-long-baseline interferometry (VLBI) technique around the earth, the EHT project forms a combined array with sufficient angular resolution to observe objects with the angular size of roughly 10 μas [31]. The participating telescopes in this project include ALMA in Chile, SMT in the USA, IRAM 30m telescope in Spain, James Clerk Maxwell Telescope in Hawaii, LMT in Mexico, SPT in the south pole, Submillimeter Array in Hawaii, NOEMA in France, KPNO in the USA, and the Greenland Telescope Project in Greenland. The primary targets for observation in this project are the black holes with the largest angular diameter as viewed from Earth, the black hole at the center of the supergiant elliptical galaxy Messier 87 (M87*), and Sagittarius A* (Sgr A*) at the center of the Milky Way.

In the case of black hole observations, the EHT uses a technique known as very-long-baseline interferometry (VLBI). In VLBI, the signals received by the telescopes are recorded and timestamped with extreme precision. The recorded signals are then transported to a central facility where they are interfered using a supercomputer. Then with the help of modeling and imaging techniques images can be produced. This technique allows the EHT to achieve an angular resolution of a few tens of microarcseconds, which is sufficient to resolve the shadow of a black hole [24, 15].

The shadow of a black hole, as we discussed earlier, is formed by the bending of light around the black hole due to its strong gravitational field. Therefore, the EHT observations opend a new window to study GR in the strong gravity limit and explore the existence of black holes and their properties, such as their mass and spin [35, 41, 16, 15].

The EHT observes frequencies ranging from 230 to 345 GHz. Within this frequency range, the apparent size of Sgr A* is approximately 50 microarcseconds (μas) [41]. As it have been mentioned earlier, the EHT possesses the capability to achieve resolutions as high as 10 microarcseconds, enabling it to resolve the event horizon of Sgr A*. Similarly, for M87, the angular size is approximately 40 μas [35], making it detectable by the

EHT. Nevertheless, capturing the intricate details of these images would prove impossible with the current measurements. There are future plans to enhance the data quality of the EHT measurements by incorporating additional telescopes worldwide, such as the next generation of EHT telescopes known as ngEHT [25]. Also, there are other plans to launch telescopes into space in order to improve the resolution, and by conducting observations at shorter wavelengths. With the addition of these telescopes, it will be possible to achieve higher-resolution observations and resolve the subsequent photon rings [61]. This would offer another means to test General Relativity and alternative theories with greater precision.

1.2.2 Gravitational Waves

Gravitational waves(GWs) were one of the early forecasts of general relativity (GR) [28] and have recently emerged as a crucial means of investigating the region near a black hole's event horizon. This significance became apparent following the discovery of GW150914 [1] by the Laser Interferometer Gravitational-Wave Observatory (LIGO). According to GR, when two black holes in a binary system begin merging, they go through three distinct stages: inspiral, merger, and ring down. During these stages, the binary system emits detectable gravitational waves, the detectability of which depends on the mass of the system. The received signal aligns with the waveform predicted by GR for the inspiral and merger of a black hole pair, as well as the subsequent ringdown of the resulting single black hole. We probe this concept more on subsection 3.5.3.

There are several other promising projects focused on detecting GWs, one of which is the International Pulsar Timing Array project. This particular endeavor combines observations of pulsars from observatories in both the northern and southern hemispheres. Its primary objective is to detect ultra-low frequency GWs, typically in the range of $10^{-9}-10^{-8}$ Hz [55]. Pulsar observations have been useful in numerous physics and astronomy breakthroughs. For instance, the first observational evidence for gravitational waves was derived from studying a pulsar-neutron star binary system [57], and pulsar observations have provided the most stringent tests of general relativity in the strong-field limit [68]. These achievements have heavily relied on a technique known as "pulsar timing." Although the details of this technique are beyond the scope of this thesis, it has been extensively described in the literature (see [67] for an overview and [56] for comprehensive methodological details).

Chapter 2

General Spherically Symmetric and Static Spacetime

Attempts to quantify the implications for potential deviations from general relativity have made use of either parameterized deviations [60, 79, 76] or explicit alternative metrics [64, 41], that we briefly reviewed them on in the introduction. Both of these approaches take strong underlying assumptions that impose strong limits on the interpretation of any results.

Parameterized metric expansions typically suffer from the inherently non-linear nature of general relativity: near the event horizon all terms in the typical expansions become similarly important, obscuring what is a limit and what is an assumption regarding the class of alternative metrics [76, 84]. Wherein these assumptions are explicitly avoided by construction [79], the resulting parameter constraints are necessarily strongly correlated — a natural consequence of a large-dimensional parameter space and a single measurement — and therefore difficult to interpret practically. Armed with strong priors, e.g., from gravitational wave experiments or theoretical arguments, this may not be catastrophic. However, given the novel nature of the EHT images of M87* and Sgr A*, and the extreme mass-scale disparity between EHT and current gravitational wave targets, there is significant value in independent gravitational tests.

Explicit alternative metrics [64] provide a physically motivated set of strong priors on the metric deviations by design, and in so doing avoid the arbitrariness associated with a parameterized model. However, these constraints are only meaningful within the context of the specific alternative metric under construction, for which the Bayesian prior is unknown and usually assumed to be small. More importantly, there is no guarantee that

neighboring metrics, i.e., "small" deviations from the alternative under consideration, are similarly constrained for the same reasons that plague parametric approaches. Hence, the results from explicit alternatives are typically only interpretable within a narrow context, requiring the onerous reconstruction of images for every metric under consideration.

Therefore, here we present an alternative scheme in which to characterize shadow size measurements that restates these in terms of direct measurements of the properties of the metric in an appropriate gauge. As such, these translate the empirical image-domain measurements performed at infinity to a gravitational domain. By casting the constraint as a measurement of the metric properties directly, this scheme has two key features:

1. It is nonparametric, thus avoiding the complications of strongly correlated parameters while maintaining the general nature of the limit.

2. It is nonperturbative, and therefore does not require any notion of "smallness" and is more naturally applicable in the highly-nonlinear near-horizon regime.

Importantly, by expressing the constraint from shadow size limits in terms of an appropriately specified metric, these are more useful to the gravitational community. It is no longer necessary to generate full images to compare with the shadow size; rather the computation of the metric components within a convenient gauge at a particular location is sufficient to bring an alternative theory into contact with the EHT and future mm-VLBI constraints.

We begin with laying out the formalism of generating shadow sizes outside of the limitation of general relativity with a general spherically symmetric metric, in this chapter. We will further make a number of convenient assumptions regarding the spacetime, each of which may be ultimately relaxed, including stationarity, axisymmetry, and slow-rotation for next chapter. We will further assume a polar observer, which is a reasonable approximation for M87* [35]. Even within this restricted classes of metrics we are able to elucidate which aspects of the spacetime remain unconstrained by a shadow size measurement.

We will not address the observational problem of measuring the shadow size, which is complicated by the fact that it is only the surrounding luminous plasma that is visible. [35] and [41] both calibrate their shadow size measurements with simulated images generated within general relativity or a narrow set of nearby alternatives, rendering interpretation of the size constraints rather more complicated. More direct methods to extract higher-order images, and therefore infer the diameter of the critical curve that bounds the shadow have been proposed [16, 61]. However, the measurement particulars and their intrinsic uncertainties are beyond the narrow scope adopted here: what would we learn from such a measurement?
Unless otherwise specified, we set $G = c = 1$.

2.1 Definitions and Properties of a General Metric

We begin with laying out the formalism of generating shadow sizes outside of the limitation of general relativity with a general spherically symmetric metric. Expressed without loss of generality in areal coordinates, the metric may be written as,

$$ds^2 = -N(r)^2 dt^2 + \frac{B(r)^2}{N(r)^2} dr^2 + r^2 d\Omega^2. \tag{2.1}$$

This metric has two arbitrary real functions of radius, $N(r)$ and $B(r)$, that set the tt and rr components of the metric. We assume asymptotic flatness, i.e., $\lim_{r\to\infty} N(r) = 1 - \mathcal{O}(1/r)$ and $\lim_{r\to\infty} B(r) = 1$. By construction, we have enforced a metric signature of $(-+++)$ throughout the region of the spacetime accessible to external observers; without loss of generality, we will further assume $N(r) > 0$ and $B(r) > 0$ everywhere in this region.

This spacetime admits two killing vector fields, and thus two constants of motion for null geodesics, which we choose to be the energy and angular momentum,

$$e = p_t = -N^2 \frac{dt}{d\tau} \quad \text{and} \quad \ell = p_\phi = r^2 \frac{d\phi}{d\tau}, \tag{2.2}$$

and due to the spacetime symmetry, all null geodesics are integrable, with the standard properties (e.g., the redshift $1 + z = N^{-1}(r)$, etc.) and live in a two spatial dimensional plane.[1] All black hole spacetimes of this form, by which we mean spacetimes with an event horizon, have $N^2(r_h) = 0$ for some horizon radius r_h by definition. Additionally, all such spacetimes also contain a photon orbit, i.e., a radius at which photons execute a circular orbit about the black hole, located at r_γ that satisfies:

$$\dot{r} = 0 \quad \text{and} \quad \ddot{r} = 0, \tag{2.3}$$

which by rearranging (2.1) for null rays ($ds^2 = 0$) gives,

$$\dot{r}^2 = \frac{1}{B^2(r)} \left[1 - \frac{b^2}{r^2} N^2(r) \right], \tag{2.4}$$

where $\dot{r} = dr/d\tau$. An effective potential, $V_{\text{eff}}(r) = N^2(r)/r^2$, may be specified in the normal way, yielding

$$\dot{r}^2 = \frac{1}{B^2(r)} \left[1 - b^2 V_{\text{eff}}(r) \right]. \tag{2.5}$$

[1] Henceforth, we will set $e = 1$ and $b = \ell/e$, which due to the assumption of asymptotic flatness is the impact parameter at infinity.

Turning points occur when $V_{\text{eff}}(r) = 1/b^2$. If $V_{\text{eff}}(r)$ has a maximum, there will be a b for which all null geodesics with smaller b will have no turning points between the event horizon and the observer at infinity. The collection of such trajectories comprise the shadow. As we mentioned before at a photon orbit, two conditions apply: $\dot{r} = 0$ (i.e., the orbit is circular) which we already discussed and $\ddot{r} = 0$ (i.e., it stays circular), and thus:

$$V'_{eff} = 0, \tag{2.6}$$

which V'_{eff} is the radial derivative of V_{eff}. Therefore:

$$r_\gamma = \frac{N(r_\gamma)}{N'(r_\gamma)}, \tag{2.7}$$

and

$$b_\gamma = \frac{1}{\sqrt{V_{\text{eff}}(r_\gamma)}} = \frac{r_\gamma}{N(r_\gamma)}, \tag{2.8}$$

also

$$\left[\frac{1}{V_{\text{eff}}(r)}\right]''_{r_\gamma} = \left[\frac{r^2}{N^2(r)}\right]'_{r_\gamma} = 0, \tag{2.9}$$

where $N'(r)$ is the radial derivative of $N(r)$. That a $r_\gamma \geq r_h$ exists that satisfies this condition follows from the assumption of asymptotic flatness and the existence of an event horizon at some finite r_h.

Note that these conditions may be satisfied at more than one location, corresponding to multiple photon orbits. That there is at least one unstable photon orbit for asymptotically flat, black hole spacetimes is guaranteed by two facts: 1. asymptotic flatness gives $V_{\text{eff}}(r) > 0$ and $V'_{\text{eff}}(r) < 0$ at very large r, and 2. $V_{\text{eff}}(r_h) = 0$ vanishes at some r_h that defines the event horizon. Thus, V_{eff} is positive and decreasing at large r and vanishes at small r, requiring via the mean value theorem that at some intermediate point $V_{\text{eff}}(r)$ has a maximum. Subsequently, photon orbits may appear in pairs, one stable (maximum of $V_{\text{eff}}(r)$) and one unstable (minima of $V_{\text{eff}}(r)$). Because the shadow is necessarily associated with the global maximum of $V_{\text{eff}}(r)$, by Equation 2.8, its size is set by the smallest b_γ. Thus, henceforth, we will restrict ourselves to the photon orbit with the smallest shadow, which we call r_γ and b_γ, respectively.

2.2 Shadows in Perturbed Spacetimes

For the innermost shadow, all null geodesics that are outward propagating at r_γ will have begun on the horizon. Thus, the boundary of the black hole shadow is associated with

those null geodesics that are tangent to the photon orbit at r_γ. This occurs when the photon angular momentum is equal to a critical value, $b_\gamma = r_\gamma/N(r_\gamma)$. Identifying b_γ with the impact parameter at infinity and using the definition of r_γ, the shadow radius is

$$R = \frac{1}{N'(r_\gamma)}. \tag{2.10}$$

As it will be shown later in the following chapter, this continues to hold unchanged for polar observers of slowly spinning black holes (i.e., up to order a, where a is the dimensionless black hole spin). As a result, there is a simple, one-to-one relationship between the observed shadow size and a property of the metric at a specific location. From this simple result a number of profound conclusions immediately follow.

2.2.1 Characterizing Shadow Size Measurements

First, because R depends solely on $N'(r_\gamma)$, $N'(r_\gamma)$ is a convenient way in which to characterize the constraints imposed by a shadow size measurement. While this may appear to be a trivial redefinition given Equation 2.10, the interpretation of $N'(r_\gamma)$ is fundamentally gravitational: it is a direct measurement of spacetime geometry at a dynamically important location for all massless fields, and thus for all electromagnetic and gravitational wave observations.

$N'(r_\gamma)$ is related to, but distinct from, $N(r_\gamma)$, a point upon which we expound below. However, it does suggest a natural framework within which to begin describing near-horizon phenomena generally:

$$N(r_\gamma),\ N'(r_\gamma),\ N''(r_\gamma),\ \ldots \tag{2.11}$$

from which the near-photon-orbit behavior of $N(r)$ can be constructed via Taylor series. Note that because R depends solely upon $N'(r_\gamma)$, for shadow size measurements this framework is nonperturbative and nonparametric.

However, characterizing strong gravity probes in this way is conceptually complicated by the unknown value of r_γ, i.e., the constrained quantity is the value of $N'(r)$ at the photon orbit, wherever that may be for a particular spacetime. While at first this may appear an onerous restriction, it is natural in that the location of the photon orbit is gauge invariant (even if the value of r_γ may not be). Explicit examples of applying this constraint will be provided in subsection 2.2.4

2.2.2 Caveats for Known Metric Expansions

As is immediately evident from Equation 2.10, there is no constraint on $N(r_\gamma)$ given a shadow size measurement. This simple fact has profound consequences for shadow size interpretations: it does not follow that because R matches its general relativistic value that $N(r_\gamma)$ should be close to its GR value. This, however, does not mean that shadow size measurements are not constraining; a tight constraint on R does indeed translate into a tight constraint on $N'(r_\gamma)$. Moreover, the detection of any shadow is a qualitative result that implies $N'(r_\gamma) > 0$, eliminating all metrics for which $N(r)$ is decreasing at r_γ. These subtleties are often lost in the context of metric expansions, for which $N(r)$ and $N'(r)$ become correlated by construction. We review some examples here.

Post-Newtonian Expansion

As we mentioned in the introduction and had been employed in [76] and in a restricted manner in [41] the Post-Newtonian Expansion of $\psi(r)$ has the form:

$$\psi(r) = \frac{\kappa_1}{r^2} - \frac{\kappa_2}{r^3} + \frac{\kappa_3}{r^4} - \frac{\kappa_4}{r^5} \dots \tag{2.12}$$

in which:

$$N^2(r) = 1 - \frac{2M}{r} + 2\psi(r), \tag{2.13}$$

where the post-Newtonian coefficients, κ_i, can be related at large r to terms in the often used parameterized post-Newtonian formalism. In this way, it is hoped that measurements of R can be related to a broad range of collected tests of general relativity on scales ranging from the laboratory to the cosmos [86, 6]

As illustrated in Figure 2.1, a perturbation defined by any single PN term traces out a curve in the $N(r_\gamma)$-$N'(r_\gamma)$ plane traversed by the associated PN coefficient. Wherein this curve lies within the band of allowed $N'(r_\gamma)$ given a measurement of R, the values of the associated κ_i are permissible, appearing to place a constraint on the magnitude of the $\psi(r_\gamma)$.

However, the addition of even a second PN term results in a band that covers the entire physically-relevant quadrant of the $N(r_\gamma)$-$N'(r_\gamma)$ plane. Thus, it appears that even with only two PN terms, no constraints are possible. This is, of course, not true: the two PN coefficients are strongly correlated, and it is within the context of that correlation, indicated rather more simply in Figure 2.1 by the gray band, that the shadow size constraint is present.

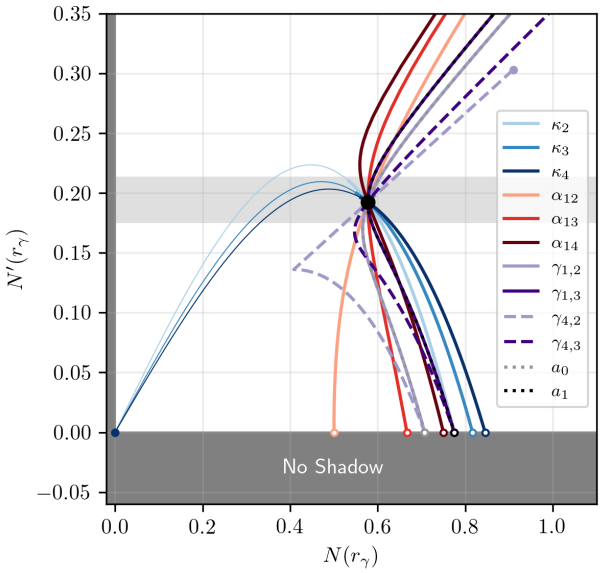

Figure 2.1: Comparison of allowed range of $N(r_\gamma)$, $N'(r_\gamma)$ for a shadow size measurement with $\sigma_R/R = 10\%$ (gray band) and the curves by single-parameter modifications to the metric. Explicitly, those associated with various PN orders, JP metric orders, MGBK metric orders for γ_1 and γ_4, and RZ metric with a_0 and a_1 varied, holding all other metric expansion parameters fixed at zero. Thin lines indicate values for which an event horizon does not exist (affecting only the PN expansion examples); the small open and filled points at which the curves terminate show when the photon orbit becomes infinite and degenerate with the event horizon, respectively. The large black point indicates the values corresponding to general relativity.

Moreover, the measurement of a shadow size does not exclude large deviations beyond r_γ. For example, consider the perturbation,

$$\psi(r) = \kappa_2 \frac{(3M - r)^2}{r^5}, \tag{2.14}$$

which is dominated by the 2PN term at $r \gg 3M$ with 2PN coefficient κ_2. This explicitly satisfies the conditions that $\psi(3M) = 0$ and $\psi'(3M) = 0$, and thus has $r_\gamma = 3M$ and $R = \sqrt{27}M$, identical to those from Schwarzschild. This is true for any value of κ_2. In this sense, there is no meaningful limit on κ_2 from any measurement of the dynamics of massless fields near the photon orbit without additional, typically strong, assumptions about the spacetime geometry.

Other Metric Expansions

For completeness, in Figure 2.1, we also show the paths traced out by the various other metric expansions considered in Section 5.1 of [41] and also had been mentioned in the introduction. These expansions include the spherically-symmetric restriction on the metrics proposed by [60, hereafter JP], MGBK [83, hereafter MGBK], and [79, hereafter RZ], as described in [41]. Each exhibits a similar qualitative behavior to the post-Newtonian expansions: the range of the inferred limits on $N(r_\gamma)$ are solely due to the priors imposed by the underlying expansion themselves. Quantitative differences are present, further highlighting the impact of these priors.

2.2.3 Comparison to Explicit Alternatives

Metrics associated with alternative gravity theories, that we mentioned some of them in the introduction, e.g., Reissner-Nordström, present a similar story as those associated with metric expansions. The details of the metric perturbation appear to induce a limit on $N(r_\gamma)$ through model-induced correlations between $N(r_\gamma)$ and $N'(r_\gamma)$. However, alternative metrics differ in an important conceptual way: the correlations are a consequence of the physical prior that the metric of interest applies and is not an arbitrary truncation of an otherwise infinite series of terms. In this sense, the constraints are meaningful within the narrow context of the alternative metric.

In Figure 2.2 we show the regions of the $N(r_\gamma)$-$N'(r_\gamma)$ plane spanned by a sample of alternative black hole metrics. Following [41], we focus attention on a subset of representative spherically-symmetric alternatives, though we expand this list to the twelve listed

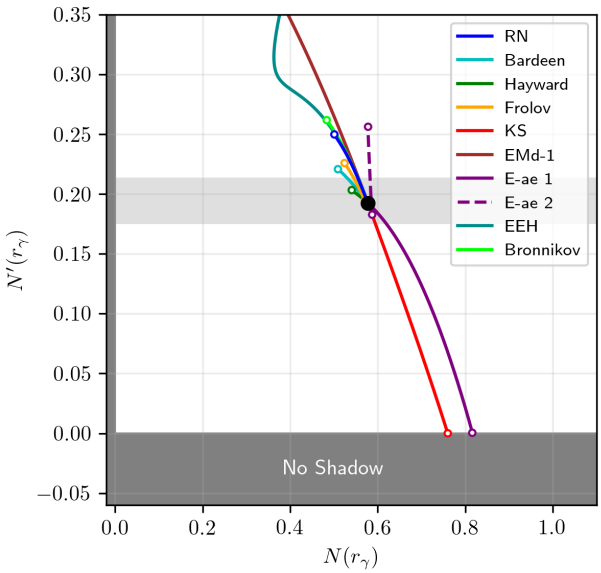

Figure 2.2: Comparison of allowed range of $N(r_\gamma)$, $N'(r_\gamma)$ for a shadow size measurement with $\sigma_R/R = 10\%$ (gray band) and the curves associated with the various axisymmetric alternative spacetimes consider in [65]. The small open points at which the curves terminate show when the charge reaches an intrinsic limit, e.g., the solution no longer has an event horizon. The large black point indicates the values corresponding to general relativity.

in Table 2.1 of [65]. We do not make any representation that these twelve are complete, but rather only that they are illustrative.[2] For more details on the metrics refer to the introduction or [41] and [65] for details on the metrics themselves and their underlying assumptions.

Two things are immediately evident upon comparison with the parameterized metric expansions. First, the imposition of physical constraints on the metric itself typically limits the region in the $N(r_\gamma)$-$N'(r_\gamma)$ plane spanned by alternative metrics significantly. In this sense, the parameterized metric expansions are more agnostic, covering a wider variety of potential deviations from general relativity. However, this is also a consequence of the difference in interpretation: where the metric expansions need to be sensible only locally, alternative spacetimes must be globally well-behaved.

Second, the general direction in the $N(r_\gamma)$-$N'(r_\gamma)$ spanned by the alternative metrics differs from those for any single-parameter exploration in the metric parameterizations in Figure 2.1. Of course, upon permitting more than one parameter to vary in the metric expansions it is possible to mimic the alternative spacetimes [65]. However, this illustrates the difficulties faced by single-parameter characterizations of the shadow-size constraints.

2.2.4 Implications of Known shadow Sizes

We now review the implications of measurements of the shadow sizes arising from EHT observations of M87* and Sgr A*. While some uncertainty regarding the methodology of such measurements may persist, we take these at face value here, and assess the implications for deviations from GR using the $N(r_\gamma)$-$N'(r_\gamma)$ formalism and more traditional metric expansions and alternatives.

2.2.5 Shadow Size Estimates

We consider four EHT shadow size measurements arising from the 2017 observing campaign, two each for M87* and Sgr A*, differing in the particulars of how they are produced. All involve two underlying measurements, that of the shadow size with the EHT and a comparison mass measurement.

[2] Where a metric depends on more than one parameter, we evaluate it at a fixed value of all but one.

2017 M87* Paper VI

First, for M87*, we adopt the angular size of the gravitational radius, i.e., $\theta_g = GM/c^2D$ where M and D are the mass of and distance to M87*, reported in [35] of $3.8 \pm 0.4\,\mu$as. Stellar dynamics measurements by [48] produce a corresponding estimate of $\theta_{\rm dyn} = 3.62^{+0.60}_{-0.34}\,\mu$as [35]. Taking the latter to define M, the former gives an estimated Shadow radius of

$$R = \sqrt{27}\frac{\theta_g}{\theta_{\rm dyn}} = \sqrt{27}\left(1.05^{+0.15}_{-0.20}\right). \tag{2.15}$$

This estimate presumes that the shadow size is indeed related to the EHT-measured size by the canonical $\sqrt{27}$, which may differ due to spin and/or the assumed astrophysics of the emitting region [49, 12]. The latter concern is amplified by the fact that the mass measurement presented in [35] calibrates the relationship between the bright ring and black hole mass using simulations that assume general relativity. Nevertheless, it forms the basis for the general relativity tests reported in [35] and [76], and thus we include it here. We refer to this shadow size measurement as the M87* 2017 Paper VI estimate in Table 2.1.

2017 Sgr A* Paper IV

Finally, for Sgr A*, we employ a similar procedure as that employed by M87* based upon the mass estimate in [39], $\theta_g = 4.8^{+1.4}_{-0.7}\,\mu$as, and the stellar dynamics measurements by [23] and [50] as collated in [41], $\theta_{\rm dyn} = 4.92 \pm 0.3\,\mu$as. The resulting estimate for the shadow size is

$$R = \sqrt{27}\frac{\theta_g}{\theta_{\rm dyn}} = \sqrt{27}\left(0.98^{+0.28}_{-0.14}\right). \tag{2.16}$$

This is significantly more conservative than the estimate from [41], with roughly twice the uncertainty. We refer to this shadow size measurement as the Sgr A* 2017 Paper IV estimate in Table 2.1.

2.2.6 Metric Expansions

The left panels of Figure 2.3 shows the implications for parameterized metric perturbations of the 2017 M87* Paper VI and 2017 Sgr A* Paper IV shadow size estimates. As in Figure 2.1, each metric parameterization imposes a strong prior within the $N(r_\gamma)$-$N'(r_\gamma)$ plane, inducing an apparent constraint on $N(r_\gamma)$ given the shadow measurement's direct constraint on $N'(r_\gamma)$.

Basis/Metric	Sole Varied Parameter	M87* 2017		Sgr A* 2017	
		Paper VI	$\theta_{n=1}$	Paper VI	Paper IV
This paper	$\sqrt{3}N(r_\gamma)$				
	$\sqrt{27}N'(r_\gamma)$	$0.95^{+0.22}_{-0.12}$	$0.89^{+0.16}_{-0.07}$	$1.04^{+0.12}_{-0.10}$	$1.02^{+0.17}_{-0.23}$
PN	κ_2	$[-2.7, 0.7]$	$[-3.2, 0.7]$	$[-0.5, 0.7]$	$[-4.2, 0.7]$
	κ_3	$[-10.9, 1.1]$	$[-13.0, 1.0]$	$[-1.7, 1.2]$	$[-17.7, 1.0]$
	κ_4	$[-44.1, 1.8]$	$[-54.1, 1.8]$	$[-5.5, 2.2]$	$[-77.6, 1.8]$
JP	α_{12}	$[-1.2, 2.0]$	$[-0.4, 2.2]$	$[-1.1, 0.5]$	$[-1.3, 2.8]$
	α_{13}	$[-3.2, 7.0]$	$[-1.1, 8.0]$	$[-3.1, 1.5]$	$[-3.5, 10.2]$
	α_{14}	$[-8.2, 26.0]$	$[-3.2, 30.5]$	$[-7.8, 4.6]$	$[-8.7, 40.5]$
MGBK	$\gamma_{1,2}$	$[-3.2, 3.2]$	$[-0.8, 3.5]$	$[-2.9, 0.9]$	$[-3.6, 4.2]$
	$\gamma_{1,3}$	$[-8.6, 11.5]$	$[-2.5, 13.1]$	$[-8.0, 2.7]$	$[-9.8, 16.2]$
	$\gamma_{4,2}$	$[-5.2, 4.0]$	$[-1.3, 4.4]$	$[-4.8, 1.3]$	$[-5.9, 5.0]$
	$\gamma_{4,3}$	$[-15.2, 13.0]$	$[-3.9, 14.3]$	$[-14.0, 3.8]$	$[-17.5, 16.8]$
RZ	a_0	$[-0.8, 0.8]$	$[-0.9, 0.2]$	$[-0.2, 0.7]$	$[-1.0, 0.9]$
	a_1	$[-1.4, 1.1]$	$[-1.6, 0.3]$	$[-0.3, 1.0]$	$[-2.0, 1.2]$
Reissner-Nordström	$0 < \bar{q} \leq 1$	< 0.86	< 0.51	< 0.84	< 0.90
Bardeen	$\bar{q}_m \leq \sqrt{16/27}$		< 0.50		
Hayward	$\bar{l} \leq 1.06$		< 1.01		
Frolov ($\bar{l} = 0.4$)	$\bar{q} \leq 0.79$		< 0.42	< 0.77	
Kazakov-Solodhukin	$\bar{a}$	< 1.65	< 1.75	< 0.79	< 1.95
EMd-1	$\bar{q} \leq \sqrt{2}$	< 0.90	< 0.51	< 0.87	< 0.94
E ae-1	$0 \leq \bar{c}_{13} < 1$	< 0.93	< 0.94	< 0.66	< 0.95
E ae-2 ($\bar{c}_{13} = 0.25$)	$0 \leq \bar{c}_{14} \leq 2\bar{c}_{13}$	< 0.33	< 0.16	< 0.31	< 0.36
CFM A	$\beta < 1$				
CFM B	$1 < \beta < 5/4$				
Bronnikov	$0 \leq \bar{c}_{13} < 1$	< 0.86	< 0.51	< 0.84	< 0.90
EEH ($\bar{\alpha} = 0.25$)	$0 < \bar{q}_m$	< 0.86	< 0.51	< 0.84	< 0.90

Table 2.1: Direct and Apparent Implications of EHT Shadow Sizes for Various Metrics
Note: For all metrics, only the parameter listed is varied. Varying multiple parameters typically results in no parameter constraint. Missing entries correspond to no constraints. See subsection 2.2.5 for how the various shadow size estimates are produced.

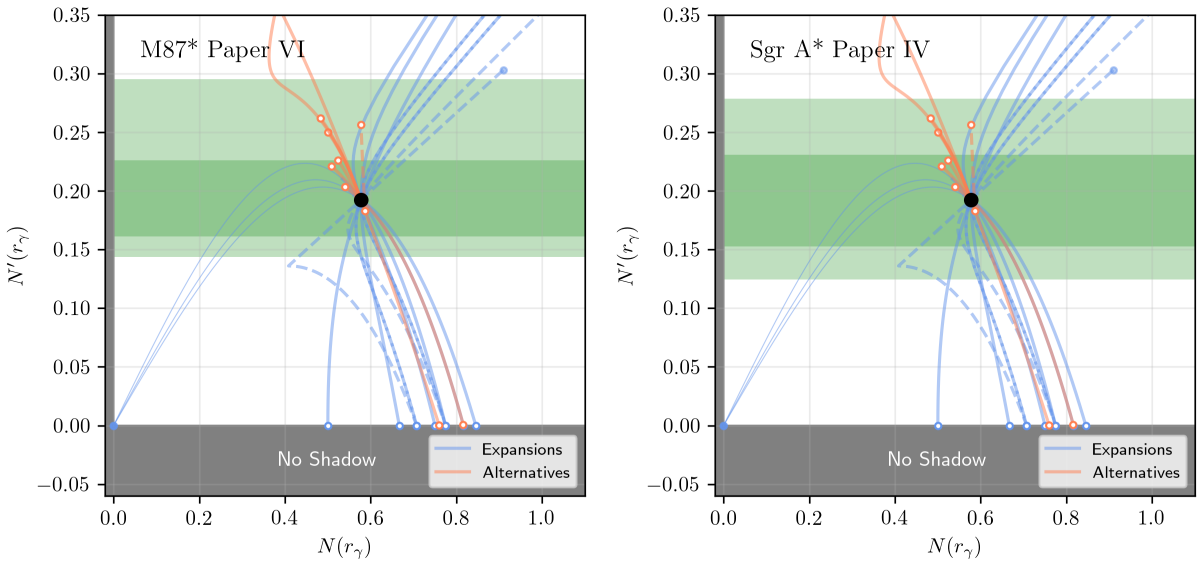

Figure 2.3: Representative constraints implied by the shadow size constraints for M87* (left) and Sgr A* (right) published by the EHT. Illustrative curves associated with the metric expansions in Figure 2.1 (blue) and alternative spacetimes in Figure 2.2 (orange) are shown. See Figure 2.1 for a description of line types. In both panels the relevant EHT measurements at 1σ and 2σ are shown by the green bands.

The 1σ single-parameter limits, when all other perturbations are fixed at zero, are collected in Table 2.1 for all four shadow size estimates. These ranges are obtained simply by inspecting the range of parameter values for which the curves in Figure 2.3 remain in the 1σ bands. Note in particular that the limits from the 2017 Sgr A* Paper VI shadow size estimates quantitatively match those in [41].[3] However, all of these limits should be interpreted with significant care for the reasons described in subsection 2.2.2. In particular, the constraint on the magnitude of the perturbation, at r_γ or otherwise, is illusory.

2.2.7 Alternative Spacetimes

The implications for the alternative metrics in [65] are shown in the right panes of Figure 2.3 for the 2017 M87* Paper VI and 2017 Sgr A* Paper IV shadow size estimates. The 1σ limits on the alternative metrics' charges are collected in Table 2.1 for all four shadow size estimates. Where appropriate, these agree with those reported in [41] and [64].

Generally, the global constraints on the alternative metrics, e.g., the necessity of an event horizon, limits the range of $N'(r_\gamma)$ permitted substantially. While not universal, this does impose a typical scale on the shadow size measurements that will be informative, roughly requiring measurement precisions of a few percent.

As with the parameterized metric expansions, limits on $N(r_\gamma)$ are inferred from the form of the particular alternative metric under consideration. Therefore, further empirical progress requires additional observables that constrain quantities other than $N'(r_\gamma)$.

2.3 Beyond Shadow Sizes

A variety of astrophysical probes of the strong-gravity regime have either already become possible, or will be possible in next decade. These are frequently relevant for ostensibly stationary spacetimes, e.g., presumably Kerr black holes, and we will consider that case. Here, we explore how multiple photon rings measurements, specifically, can incorporate into measurements of $N(r_\gamma)$, $N'(r_\gamma)$, etc., and what additional underlying assumptions may be necessary.

The shadow is bounded by an infinite sequence of higher-order images of the accretion flow, often referred to as "photon rings". Each higher-order photon ring is the result of

[3] A solitary exception is the constraint on $\gamma_{1,2}$ of the MGBK expansion. However, the values in Table 2.1 quantitatively match those inferred from Fig. 17 of [41], and thus we attribute the mismatch to a typographical error in Table 3 of [41].

an additional half-orbit executed by the null geodesic prior to streaming toward a distant observer. Necessarily, each ring is distinctly located in the image (no position in the image can contribute to more than one null geodesic, and, therefore, more than one image). These are purely geometric features, depending only upon the strong lensing within the spacetime, and therefore present a natural probe of general relativity [16].

The ability to separate and extract individual ring-like structures within images has recently been developed [15, 14] and future experiments may be able to resolve multiple such rings [61, 16]. Thus, measuring the size of multiple photon rings presents a natural and practical extension to the notion of measuring the shadow size, and is necessarily probing the region near the photon orbit.

Similar to the way that been discussed in the introduction to find the multiple photon rings for Schwartzshild and Kerr spacetime, one can derive the multiple photon rings for this general spherically symmetric space time. The higher order images of the near-horizon emission region form a sequence of typically ring-like image features [13, 61, 16]. Each additional image is associated with photon trajectories that execute an additional half orbit about the black hole, and therefore the size of these rings are probes of spacetime about the photon orbit. Here we derive the radius of the higher-order photon rings in the limit of high photon-ring order.

For null geodesics near the photon orbit, i.e., for which

$$r = r_\gamma + \delta r, \tag{2.17}$$

Equation 2.4 becomes after Taylor expanding about $r = r_\gamma$ to lowest order,

$$\dot{\delta r}^2 \approx -\frac{b_\gamma^2}{2B^2(r)} \left[\frac{N^2(r)}{r^2}\right]''_{r_\gamma} \delta r^2, \tag{2.18}$$

where the first two terms vanish due to Equation 2.8 and Equation 2.9 and because the inner turning point (i.e., the minimum δr) is small, we've replaced b with b_γ. Combining this radial equation of motion with Equation 2.2, gives

$$\pi \frac{d\delta r}{d\phi} = \gamma \delta r, \tag{2.19}$$

where

$$\gamma = \pi \frac{N^{3/2}(r_\gamma)}{N'(r_\gamma)} \left[-\frac{N''(r_\gamma)}{B^2(r_\gamma)}\right]^{1/2}, \tag{2.20}$$

is the Lyapunov exponent identified in [61]. Solving this, we obtain,

$$\delta r = \delta r_0 e^{\gamma\phi/\pi}, \tag{2.21}$$

i.e., upon every half orbit the geodesic grows by a factor of e^{γ}. This matches Equation 7 of [61] in the limit of Schwarzschild.

At some $\delta r_{\rm max} \sim M$, the perturbative expansion of the radial equation of motion breaks down, and the photon trajectory streams to the observer at infinity. Prior to this point, it will have executed

$$n \approx \frac{2}{\pi}\gamma^{-1} \ln\left(\delta r_{\rm max}/\delta r_0\right), \tag{2.22}$$

half orbits, where the preceding orbits from a distant source to the vicinity of the photon orbit are now included, and thus contribute to the nth-order photon ring. Describing the details of the transition is not necessary to obtain the relative locations of the photons on a distant observing screen; rather the photon ring sizes are completely controlled by b, which is, in turn, set by the inner turning point, i.e., by δr_0. At δr_0, $\dot{r} = 0$, and therefore,

$$b^2 \approx b_\gamma^2 + \frac{1}{2}\left[\frac{r^2}{N^2(r)}\right]''_{r_\gamma} \delta r_0^2, \tag{2.23}$$

where again the linear term vanishes as a result of Equation 2.9. Identifying the radius of the nth order photon ring, R_n, with the b associated with the δr_0 that corresponds to n half orbits, we find

$$R_n - R \approx \frac{N'(r_\gamma)}{4}\left[\frac{r^2}{N^2(r)}\right]''_{r_\gamma} \delta r_{\rm max}^2 e^{-\gamma n}. \tag{2.24}$$

The prefactor is common to all order photon rings. The shift relative to the shadow size decreases as $e^{-\gamma n}$, from which we recover that the shadow is bounded by the asymptotic photon ring corresponding to $n \to \infty$. This matches Equation 12 of [61].

Therefore, it's been estimated that the radii of high-order photon rings relative to that of the shadow is,

$$R_n - R \approx h e^{-\gamma n}, \tag{2.25}$$

where h is a function of r_γ, $N(r_\gamma)$, $N'(r_\gamma)$, and $N''(r_\gamma)$. Note that in addition to $N(r_\gamma)$ and $N'(r_\gamma)$, γ depends on $N''(r_\gamma)$ and $B(r_\gamma)$ through the combination $N''(r_\gamma)/B^2(r_\gamma)$. This is a consequence of the fact that the finite order photon ring radii are dictated by the dynamics of photons very nearby, but outside of the photon orbit. Because γ also describes the rate at which the radii of these trajectories grow, it naturally depends on the second derivative of the effective potential, $N''(r_\gamma)$, and the notion of radial distance, $B(r_\gamma)$, at r_γ.

The absolute normalization must ultimately be computed numerically and may differ among spacetimes. However, the relative sizes are fully fixed by γ, and thus it is possible to measure γ directly with a shadow size and two photon ring radii:

$$\gamma = \ln\left(\frac{R_n - R}{R_{n+1} - R}\right). \tag{2.26}$$

Alternatively, measuring three photon ring radii permits removing R altogether,

$$\gamma = \ln\left(\frac{R_{n+1} - R_n}{R_{n+2} - R_{n+1}}\right). \tag{2.27}$$

As with the detection of a shadow, the detection of a single photon ring has profound qualitative implications, requiring $N''(r_\gamma)$ to be positive.[4] Otherwise, the photon orbit would be stable, and the associated null geodesics not reach distant observers to generate a ringlike structure in the images.

Examples of the implications of a 10% measurement of γ are shown in Figure 2.4, roughly the precision required to distinguish the $n = 1$ and $n = 2$ photon rings. Because measurements of γ are necessarily coupled with a high-precision measurement of R, $N'(r_\gamma)$ is effectively fixed, resulting in an additional constraint in the $N(r_\gamma)$-$N''(r_\gamma)/B^2(r_\gamma)$ plane. The qualitative differences between the interpretation of such a measurement for parameterized metric expansions and explicit metric alternatives is similar to that for the shadow size. The measurement presents a fundamentally degenerate constraint. Thus, even multiple photon ring measurements, it is not possible to uniquely determine $N(r_\gamma)$.

[4]More properly, positive in an appropriate neighborhood of r_γ, the size of which depends on the particular order photon ring under consideration.

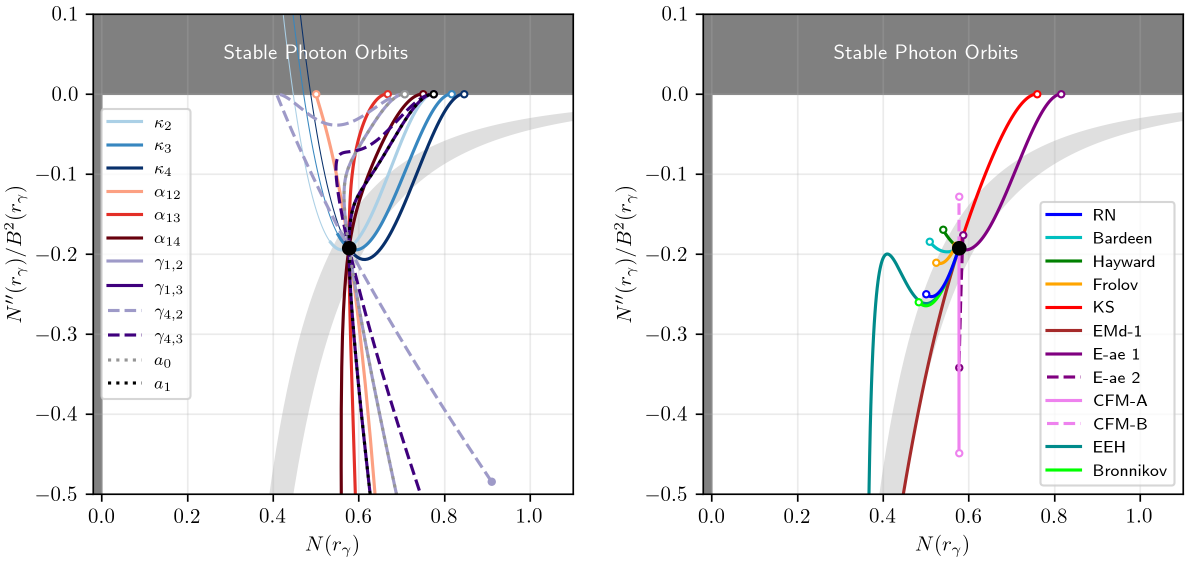

Figure 2.4: Constraints on $N''(r_\gamma)/B^2(r_\gamma)$ arising from a 10% measurement of γ. For reference, the curves associated with parameterized metrics (above) and alternative theories (below) are shown. Line types and points are the same as in Figure 2.1 (above) and Figure 2.2 (below).

Chapter 3

General Axi-symmetric and Stationary Spacetime

In the previous chapter, we examined how modifications to a general static and spherically symmetric metric would affect the shadow size and multiple ring measurements. In this current work, we expand on that approach and explore a stationary and axisymmetric metric, similar to the Kerr spacetime.

Despite the increased complexity of this spacetime, we maintain the two key features of our previous work: a non-parametric metric to retain generality and avoid complications from strongly correlated parameters, and a non-perturbative metric for better applicability in the highly-nonlinear near-horizon regime.

We construct the metric and explore the existence of the shadow and subsequent photon rings, calculating their respective sizes and radii. We also define the Lyapunov exponent for these rings and discuss its measurement, which helps to constrain the metric components. Additionally, we investigate the simplified cases of slow rotation and polar observer independently here.

3.1 The Polar Observer in General Spherically Symmetric Spacetimes

We start by mentioning an important fact about spherically symmetric spacetimes that would be helpful later. Spherical symmetry renders the problem of computing orbits planar.

As a consequence, it is typical to compute orbits in the equatorial plane. However, because the situation of practical interest here are polar orbits about axisymmetric spacetimes, this simplification is no longer possible. Before discussing the general case, we begin by demonstrating the equivalence of such a calculation in the spherically symmetric case, introducing the relevant constants of motion, and providing an explicit example of their use.

3.1.1 Polar Photon Orbits

Here we repeat the computation that we had in the previous chapter for equatorial orbits, but in a language explicitly relevant for polar orbits. Again, we require two constants of motion, the first of which will be the energy, e. The second is now given by the Carter constant,

$$Q = p_\theta^2 + L_z^2 \cot^2\theta, \tag{3.1}$$

which for orbits with $L_z = 0$ reduces to $Q = p_\theta^2$. We define $q \equiv \sqrt{Q}/e$, and the equations of motion for the polar trajectories (with $L_z = 0$) are

$$\dot{r}^2 = \frac{e^2}{N^2}\left(1 - \frac{q^2}{r^2}N^2\right) \quad \text{and} \quad \dot{\theta} = e\frac{q}{r^2}, \tag{3.2}$$

which apart from replacing one constant for another (q for ℓ) is identical to (2.2). It immediately follows that $r_\gamma = N(r_\gamma)/N'(r_\gamma)$ and $q = 1/N'(r_\gamma)$. As before(section 2.2), for polar observers, q may be identified with the impact parameter for photon orbits that reach observers at infinity.

The shadow is surrounded by an infinite series of higher-order images, i.e., the "photon rings". Each subsequent order ring is associated with an additional half-orbit made by the null geodesic before it heads towards a faraway observer. As each ring is situated at a unique position in the image, no position can produce more than one null geodesic or image. These features are solely based on the strong gravitational lensing within the spacetime and serve as an excellent tool to investigate general relativity. In order to explore these rings we calculate the Lyapunov exponent like we did before. Using (3.2) and expanding around r_γ we have:

$$\dot{\delta r}^2 \approx -\frac{q}{2B^2(r)}\left[\frac{N^2(r)}{r^2}\right]''_{r_\gamma}\delta r^2, \tag{3.3}$$

then by utilizing the definition of the Lyapunov exponent:

$$\pi\frac{d\delta r}{d\phi} = \gamma\delta r \tag{3.4}$$

we get:

$$\gamma = \pi \frac{N^{3/2}(r_\gamma)}{N'(r_\gamma)} \left[-\frac{N''(r_\gamma)}{B^2(r_\gamma)} \right]^{1/2} \tag{3.5}$$

that is exactly what we had before for the orbits in equatorial plane of the spherical spacetime, which was expected due to the spherical symmetry of the spacetime.

This illustrates the general procedure we will follow here, and the role that the Carter constant will play, analogous to that of angular momentum in the spherical context.

3.2 A General Non-Parametric Non-Perturbative Axisymmetric spacetime

The Kerr metric is an exact solution to the vacuum Einstein field equations, and describes spinning black hole spacetimes. It is the sole uncharged stationary, axisymmetric, asymptotically flat, nonpathological solution to the the Einstein equations, and therefore is believed to be applicable to astrophysical black holes.[1]

Due to the presence of two clear symmetries that involve stationarity and axisymmetry, test particles possess two conserved quantities, namely energy and angular momentum along the rotation axis, as a result of Noether's theorem. Less obvious is the presence of a third integral of motion, the Carter constant ([18]). In addition to a fourth constant, particle rest mass, test particle orbits in Kerr are fully integrable.

In contrast, deviations from Kerr need not admit fully integrable geodesics. Nevertheless, their obvious utility has motivated the definition of a broad family of arbitrary stationary, axisymmetric metrics that have four constants of motion [60]. By construction, this set of metrics possesses a modified Carter constant, allowing us to avoid concerns about the integrability of the spacetime and simplifying the examination the path of photons around the central mass. These metrics introduces four arbitrary real functions of radius (called $A_1(r)$, $A_2(r)$, $A_5(r)$, and $f(r)$ in [60]) that we will not expand upon and will leave in their general form. Consequently, we extend the proposal of a nonperturbative, nonparametric characterization of shadow size and related measurements in the spacetime domain in the previous chapter to a broad class of spinning spacetimes, explicitly demonstrating the nature and effectiveness of shadow size-based constraints.

[1] While the Kerr-Newman metric, which describes the charged black holes, presents a more general class of spacetime, the abundance of free charges in astrophysical environments precludes this possibility in practice.

We begin with a manifestly stationary and axisymmetric metric, expressed in terms of four arbitrary functions of radius, $N(r)$, $B(r)$, $F(r)$, and $f(r)$,

$$ds^2 = -\frac{\tilde{\Sigma}N^2}{(r - Fa^2\sin^2\theta)^2}(dt - a\sin^2\theta d\phi)^2 + \frac{\tilde{\Sigma}\sin^2\theta}{(r - Fa^2\sin^2\theta)^2}(aFdt - rd\phi)^2 + \tilde{\Sigma}\frac{B^2}{N^2}dr^2 + \tilde{\Sigma}d\theta^2, \tag{3.6}$$

where

$$\begin{aligned} \tilde{\Sigma} &= r^2 + a^2\cos^2\theta + f(r) \\ \Delta &= r^2 - 2Mr + a^2, \end{aligned} \tag{3.7}$$

and the parameters M and a are parameters related to the mass and spin[2]. This is identical to the metric presented in Equation 51 of [60] (see Appendix H).

Expressing from [60] family of metrics in this fashion has some significant conceptual benefits.

1. The event horizon for stationary spacetimes, defined by where g_{rr} diverges, occurs at the largest radius for which $N(r) = 0$. That is, $N(r)$ completely describes the location and structure of the event horizon; that an event horizon exists reduces to the requirement that $N(r)$ has at least one root. Furthermore, the event horizon is necessarily at fixed r, i.e., within our particular choice of coordinates (which reduce to Boyer-Lindquist in Kerr), the horizon appears spherically symmetric.

2. The ergosphere, defined by where g_{tt} vanishes, is set by

$$N^2(r) - a^2F^2(r)\sin^2\theta = 0, \tag{3.8}$$

   and thus its structure is determined by $F^2(r)$ once $N^2(r)$ is specified, with immediate consequences for the existence and structure of the ergosphere. When $a = 0$, Equation 3.8 is never satisfied outside of the event horizon, and there is no ergosphere. Similarly, when $F(r) = 0$, there cannot be an ergosphere. Thus, within this family of metrics, the spin and $F(r)$ must be non-zero for energy extraction via the Penrose process and related mechanisms [74]. There is also a strong constraint on the poloidal shape of the ergosphere. Because $N^2(r)/F^2(r)$ is a function of r alone, the shape of the boundary of each ergosphere depends only the magnitude of the black hole spin (as it must be) and is axi-symmetric.

[2] M and a are exactly the ADM mass and spin when $N(r)$, $B(r)$, $F(r)$, and $f(r)$ take on appropriate asymptotic behavior at large r (see Appendix G).

3. When $a = 0$, $N(r)$ and $B(r)$ take on the same meaning as they did in chapter 2. For polar observers, we shall see they take on the same importance for the shadow and photon ring sizes.

The first two constants of integration of photon trajectories are given by their usual expressions, $e \equiv p_t$ (which we set to unity) and $L_z = p_\phi = \ell e$. The third constant of motion is the modified Carter constant, which for photons is by construction,

$$Q = p_\theta^2 + \frac{(\ell - a\sin^2\theta)^2}{\sin^2\theta} - (\ell - a)^2. \tag{3.9}$$

For polar observers, to which we will restrict ourselves, the Carter constant reduces to $Q = p_\theta^2 - a^2$, which, as in the sphercally symmetric case, we will again express in terms of $q \equiv \sqrt{\frac{Q}{e^2}}$.

3.3 Polar Shadow Size

As seen by a distant observer located along the polar axis, the image of the event horizon (or the photon orbit) fills a circle. The location of photon trajectories on a screen at large r asymptotes to,

$$R = M\sqrt{q^2 + (\ell - a)^2 - (\ell - a\sin^2\theta)^2/\sin^2\theta}, \tag{3.10}$$

(see [20]). We will consider only orbits with $L_z = 0$, which corresponds to a screen that is not rotating at infinity, for which R reduces to

$$R = M\sqrt{q^2 + a^2}, \tag{3.11}$$

reducing the problem of determining the shadow size to identifying the Carter constant of those photons that just graze the photon sphere, the generalization of the unstable circular photon orbit from the spherically symmetric case.

The equation of motion of the photons near the black hole is given in Equation 35 of [60], which expressed in terms of our metric functions becomes,

$$\dot{r}^2 = \frac{r^2}{\tilde{\Sigma}^2}\frac{1}{B^2(r)}\left[1 - \frac{q^2 + a^2}{r^2}N^2(r)\right], \tag{3.12}$$

which differs from the spherically symmetric case only by a prefactor. On the unstable photon sphere, we again require $\dot{r} = 0$ and $\ddot{r} = 0$. The first condition is satisfied outside the event horizon when $q_\gamma^2 + a^2 = r_\gamma^2/N^2(r_\gamma)$. The second requires

$$r_\gamma = N(r_\gamma)/N'(r_\gamma), \tag{3.13}$$

(see section F.1). As the name photon sphere implies, in these coordinates, these orbits all lie at constant radius. Substituting these two conditions in Equation 3.11 gives

$$R = \frac{M}{N'(r_\gamma)}. \tag{3.14}$$

Note that these expressions are *identical* to those for the spherically symmetric spacetime, and thus $N(r)$ plays an exactly analogous role in the family of integrable stationary axisymmetric spacetimes for polar observers. Similar to the spherically symmetric scenario, the identification of the shadow relies solely on the value of N' at r_γ. Consequently, any measurements of shadow size do not provide additional information about other arbitrary functions of the general metric, such as B or F. The former implies that shadow size measurements do not necessarily offer insights into the g_{rr} component of the metric and, consequently, radial distances. The latter indicates that the determination of the ergosphere's location using shadow size measurements is not possible, as F is the determining factor for the ergosphere, as mentioned earlier. Therefore, we do not see evidence of frame dragging via shadows or multiple photon rings. We are going to show the latter in the following section. However, it is worth mentioning again that the shadow size measurement does provide an evidence for existence of a real positive value of N' at r_γ.

3.4 Multiple Photon Rings

The shadow is surrounded by an infinite series of photon rings, composed of higher-order images. These rings are created by the null geodesic's execution of an additional half-orbit before moving towards a faraway observer. These features are geometric and depend soley on strong gravitational lensing, making them an excellent tool for studying general relativity in the vicinity of the photon orbit.

Higher order photon rings lie exponentially closer to the shadow boundary, with their structure heavily impacted by the dynamics of orbits nearby r_γ. To examine the radii of the photon rings, we will make the following assumptions regarding their propagation:

1. Each photon ring has an inner turning point at some radius outside of the photon sphere, $r_\gamma + \delta r_0$.

2. This location is sufficiently close to the photon sphere that we may perturbatively expand the photon equation of motion about r_γ.

3. Upon propagating some distance of order M away from r_γ, the photon will stream to the observer at infinity.

The second provides an immediate equation of motion for δr, obtained from expanding Equation 3.12 about r_γ,

$$\dot{\delta r}^2 = -\frac{r^2}{\tilde{\Sigma}^2}\frac{(q^2+a^2)}{2B^2(r)}\left[\frac{N^2(r)}{r^2}\right]''\Big|_{r_\gamma}\delta r^2. \tag{3.15}$$

Again, apart from prefactors, this is very similar to the expression found in the spherically symmetric case. Importantly, it is proportional to $R^2[N^2(r)/r^2]''$.

Unlike the spherically symmetric case, this now depends on the polar angle via $\tilde{\Sigma}$. However, the angular equation of motion at constant r is

$$\dot{\theta} = p^\theta = \frac{1}{\tilde{\Sigma}}\sqrt{q_\gamma^2 + a^2 - a^2\sin^2\theta}, \tag{3.16}$$

which the $\tilde{\Sigma}$ terms would canceled out and thus,

$$\frac{d\delta r}{d\theta} = G(\theta)\frac{N^{3/2}(r_\gamma)}{N'(r_\gamma)}\left[-\frac{N''(r_\gamma)}{B^2(r_\gamma)}\right]^{1/2}\delta r, \tag{3.17}$$

where

$$G(\theta) \equiv \frac{R}{\sqrt{R^2 - a^2\sin^2\theta}}. \tag{3.18}$$

We note that $G(\theta)$ is independent of the four metric perturbations, apart from the specification of R. Therefore, we may integrate Equation 3.17 immediately to obtain that the growth in orbital radius from the n to $n+1$ half orbit is

$$\ln\left(\frac{\delta r_{n+1}}{\delta r_n}\right) = \frac{N^{3/2}(r_\gamma)}{N'(r_\gamma)}\left[-\frac{N''(r_\gamma)}{B^2(r_\gamma)}\right]^{1/2}\int_0^\pi d\theta G(\theta). \tag{3.19}$$

Expressing this in terms of the orbital radius at the inner turning point, the orbital radius after n half-orbits is

$$\delta r_n = \delta r_0 e^{\gamma n} \tag{3.20}$$

in which the Lyapunov exponent is given by

$$\gamma \equiv \frac{N^{3/2}(r_\gamma)}{N'(r_\gamma)}\left[-\frac{N''(r_\gamma)}{B^2(r_\gamma)}\right]^{1/2} 2K[(a/R)^2] \tag{3.21}$$

where $K(k)$ is the complete elliptic integral of the first kind. Identically, when $a = 0$, we have $K[(a/R)^2] = \pi/2$ and γ reduces to the expression (2.20) in chapter 2.

The requirement that there is an inner turning point at $r = r_\gamma + \delta r_0$ modifies the Carter constant associated with the photon ring trajectories. Because $\dot{r} = 0$ on the photon sphere, the lowest order at which q changes is second order, i.e.,

$$q^2 + a^2 = q_\gamma^2 + a^2 + \frac{1}{2}\left[\frac{r^2}{N^2(r)}\right]''_{r_\gamma} \delta r_0^2. \tag{3.22}$$

Employing the third assumption, that upon reaching some radius $(r_\gamma + \delta r_{\max})$ the photon streams toward infinity, we may estimate the radii of the photon rings generated by n half orbits (i.e., $\theta = n\pi$),

$$R_n - R \approx \frac{N'(r_\gamma)}{4}\left[\frac{r^2}{N^2(r)}\right]''_{r_\gamma} \delta r_{\max}^2 e^{-\gamma n}, \tag{3.23}$$

which is identical to the spherically symmetric case up to the generalization of γ. By measuring the radii of three photon rings, it becomes possible to eliminate the need for the shadow size altogether,

$$\gamma = \ln\left(\frac{R_{n+1} - R_n}{R_{n+2} - R_{n+1}}\right). \tag{3.24}$$

As previously stated within this section, the shadow is constrained by these multiple photon rings. The observation of the shadow serves as evidence for the presence of a real and positive value for γ. According to equation (3.21), this implies a requirement for a positive value of $-N''/B^2$. In the following section we will discuss more about other constraints that the shadow size measurement and other possible measurements can put on the metric components.

3.5 Constraints on the Metric by Observation

In this section, we examine the consequences of the EHT's measurements of the shadow sizes of M87*, which is viewed nearly face on. Although there is some uncertainty in the measurement approach (see subsection 2.2.5), we accept the results at face value and evaluate their implications for deviations from gravity using both the $N(r_\gamma)$-$N'(r_\gamma)$ formalism and alternatives.

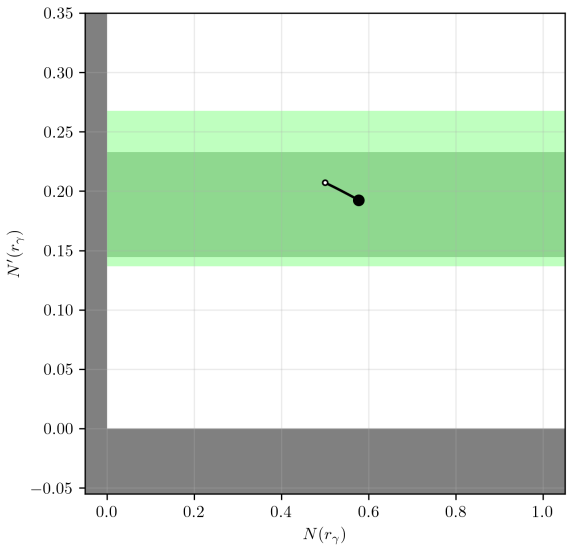

Figure 3.1: $N - N'$ plot for Kerr spacetime

Representative constraints implied by the shadow size measurements for M87*, that had been mentioned in subsection 2.2.4, at 2σ, is represented by the green shaded regions. The solid black line demonstrates valid regions for Kerr spacetime. Additionally, the black dot illustrations the Schwarzschild value. Also, the dark grey shaded region, are excluded due to the existence of shadow(see section 3.3).

3.5.1 Observational Implications on Kerr Spacetime

In order to gain a better understanding of the procedure, we first examine the observational implications of Kerr spacetime before delving into the implications for alternative metrics. As discussed in section 3.3, the size of the shadow is directly determined by the value of N' at r_γ, without imposing any constraint on the value of N at that location. However, in the case of assuming the spacetime to be Kerr, there exists a relationship between N and N' derived from the underlying theory, which allows for constraints on both variables. A visual representation of this concept can be seen in Figure 3.1. The N-N' diagram at r_γ for various spin values is depicted by the black curve, illustrating how Kerr spacetime aligns with the shadow size measurements of M87 discussed in subsection 2.2.4. This plot clearly demonstrates that Kerr spacetime is entirely encompassed within the current EHT measurements. To effectively distinguish between various spins with a precision of $\delta a = 0.1$, the required level of accuracy is approximately four orders of magnitude smaller than the current observation range for the shadow size.

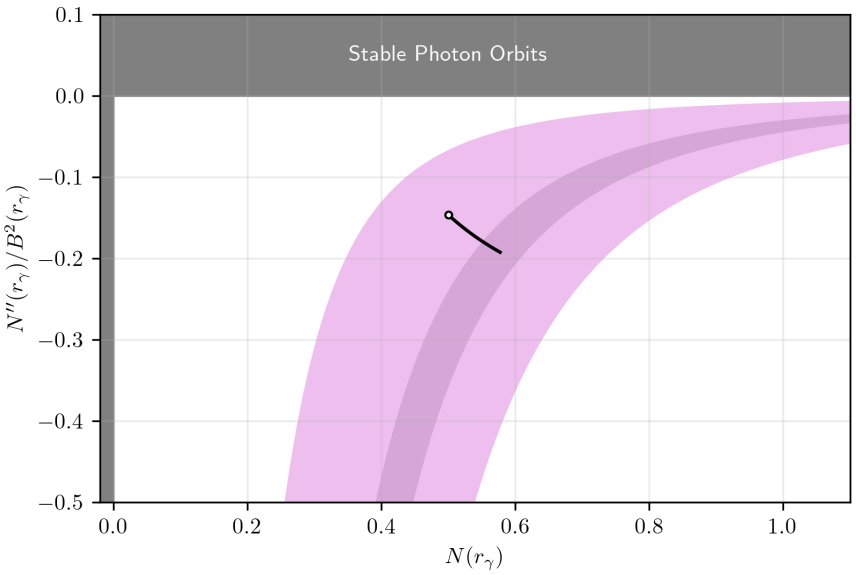

Figure 3.2: $N - N''/B^2$ diagram for Kerr spacetime

Representative constraints implied by the QNM measurements, that had been mentioned in [2], at 2σ, is represented by the pink shaded region (also see subsection 3.5.3 for some detail). The black dot illustrations the Schwarzschild value. The solid black curve shows the Kerr spacetime for different value of spin. Also, the dark grey shaded region, is excluded due to the existence of shadow (see section 3.4).

Furthermore, an additional means of testing the underlying theory, here GR, involves utilizing measurements of the Lyapunov exponent in potential future observations of the photon rings. Please refer to Figure 3.2 for a visual representation of the acceptable range of Kerr spacetime corresponding to different spin values. It is worth noting that the shaded regions in the $N - (N''/B^2)$ plane is obtained by inserting the various measurements of N' from the M87 observations in subsection 2.2.4 into Equation 3.21 for Kerr spacetime. This plot provides clear evidence that Kerr spacetime is fully encompassed by the current QNM measurements (see subsection 3.5.3 and [2]). In order to differentiate between different spins with a precision of $\delta a = 0.1$, the necessary level of accuracy is roughly two orders of magnitude smaller than the current observation range for the Lyapunov exponent, which will be further discussed in Section (3.5.3).

3.5.2 Observational Implications on Alternative Spacetimes

The current measurements of the EHT shadow size provide an opportunity to assess alternative theories of gravity in addition to general relativity.(see subsection 2.2.5) Instead, our focus lies on the theoretical implications of the model-agnostic framework introduced in this study, aiming to test alternative metrics that are compatible with equation (3.6).

Figure 3.3 and Figure 3.4 illustrate the permissible region for $N - N'$ and $N - N''/B^2$ at r_γ in various alternative spacetimes mentioned in Appendix J and Appendix J. By utilizing the shadow size measurements, these plots enable the exclusion of certain spin and extra charge values associated with these alternatives, thereby imposing constraints on them. Moreover, as we discussed before, the existence of a shadow implies a positive value for N' and $(-N''/B^2)$ at r_γ(see section 3.3 and section 3.4). This fact excludes the lower half plane of the $N - N'$ and upper half of the $N - (N''/B^2)$. Additionally, without loss of generality we can assume N is positive and therefore exclude the left half of these diagrams.

As we discussed on chapter 2 by utilizing both shadow size measurement and potential future measurements of photon rings radii, one can establish limitations on the values of free parameters in the underlying theory. To illustrate this idea, several lines in Figure 3.3 and Figure 3.4 depict varying values of these free parameters. The blue lines correspond to a constant spin value for different values of an additional charge used in these theories to explain gravity. Conversely, the red lines represent a constant extra charge for different spin values.

3.5.3 LIGO measurements

With the detection of GW150914, gravitational waves have become an important probe of the near-horizon region of merging stellar-mass black holes. Future space-based interferometers [3] and pulsar timing monitoring experiments promise to expand these tests to supermassive black holes that are directly comparable to EHT observations of Sgr A* and M87*, respectively[55].

Comparison of these limits is complicated by the fact that gravitational wave observations necessarily require specification of the dynamical sector of any putative gravity theory. Therefore, it is generally insufficient to postulate alternative stationary spacetimes as doing so does not inform dynamical phenomena of any alternative theory. With this caveat, there are two situations in which it may nevertheless be useful to characterize

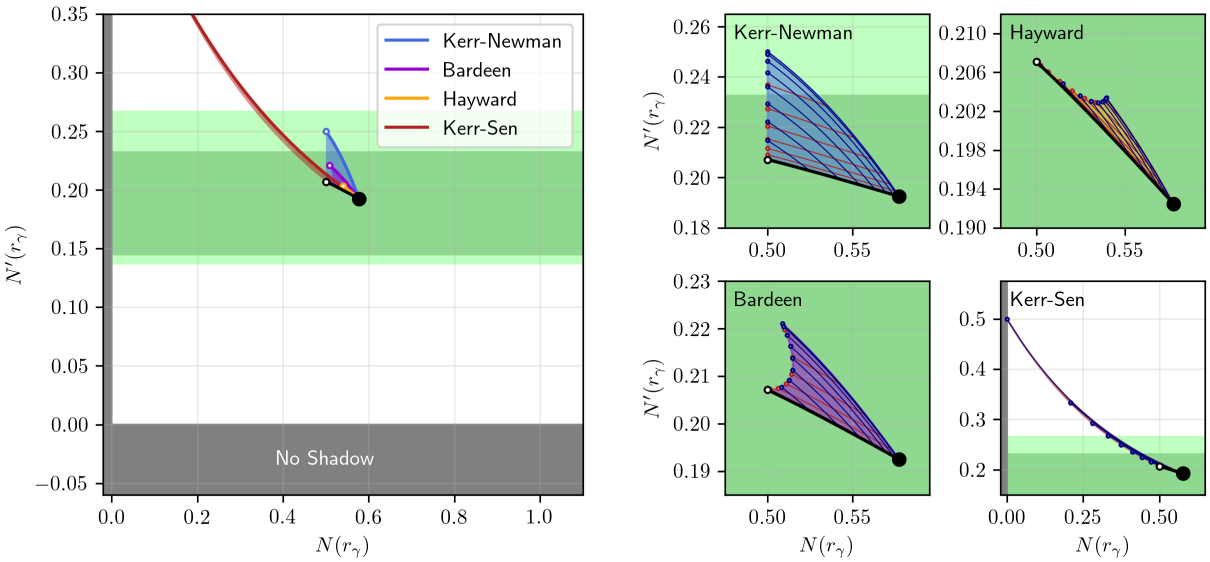

Figure 3.3: $N - N'$ diagram for alternative spacetime

Representative constraints implied by the shadow size measurements for M87*, that had been mentioned in subsection 2.2.4, at 2σ, is represented by the green shaded regions,in these diagrams. In all of the plots, the colored regions demonstrates valid regions for alternative spacetimes. Additionally the black dot illustrations the Schwarzschild value. The black curve shows the Kerr spacetime for different value of spin. Also, the dark grey shaded regions, in both plots, are excluded due to the existence of shadow(see section 3.3 and section 3.4). On the left side, you can see more elaborate representations of the plots, for these metrics .

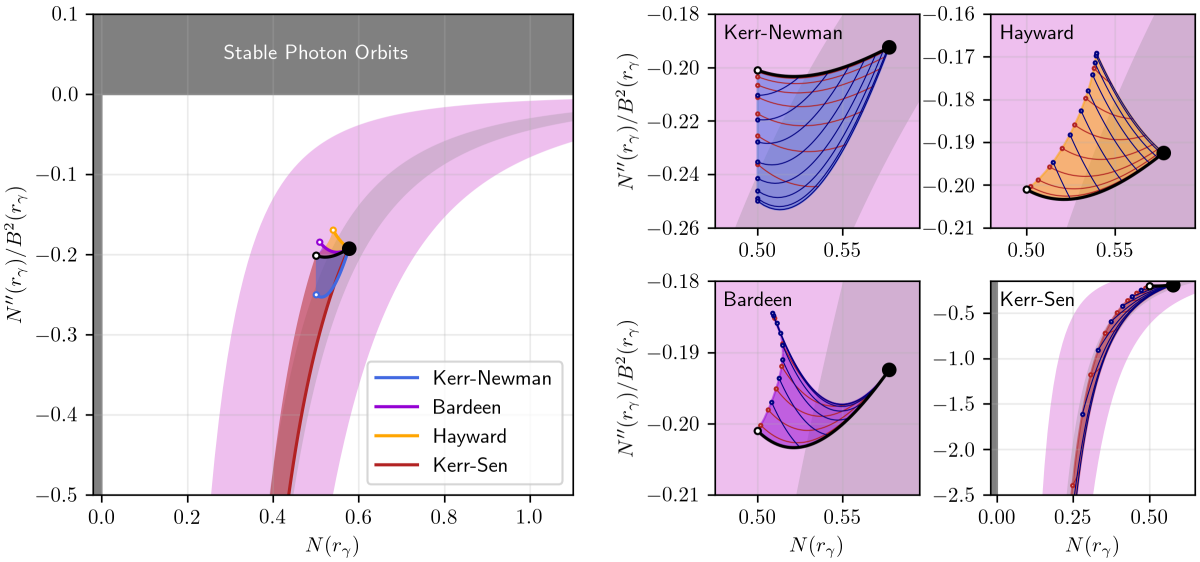

Figure 3.4: $N - N'$ diagram for alternative spacetime

Representative constraints implied by the QNM measurements, that had been mentioned in [2], at 2σ, is represented by the pink shaded regions, in these diagrams(also see subsection 3.5.3 for some detail). In all of the plots, the colored regions demonstrates valid regions for alternative spacetimes. Additionally the black dot illustrations the Schwarzschild value. The black curve shows the Kerr spacetime for different value of spin. Also, the dark grey shaded regions, in both plots, are excluded due to the existence of shadow(see section 3.3 and section 3.4). On the left side, you can see more elaborate representations of the plots, for these metrics .

results in the way proposed here: gravitational wave ringdowns and extreme mass ratio inspirals (EMRIs), which we treat in turn.

Gravitational Wave Ringdown

The late-time evolution of high-angular momentum quasinormal modes (QNMs) is related in general relativity to the shadow size [62, 81, 89]. This is a consequence of these modes being associated with high-frequency, azimuthally propagating massless perturbation, which is necessarily governed by the same dynamics as photons near the photon orbit. As a consequence, generically the angular frequency, $\omega = \omega_{R,l} + i\omega_{I,l}$ of the quasinormal mode with azimuthal quantum number l is given by [3]

$$\lim_{l\to\infty} \omega_{I,l} = \frac{N'(r_\gamma)\gamma}{2\pi} \quad \text{and} \quad \lim_{l\to\infty} \frac{\omega_{R,l}}{l} = N'(r_\gamma), \tag{3.25}$$

which are equivalent to Equation I.1 of [89]. Thus, observations of high-frequency quasinormal modes result in spacetime constraints that are directly comparable to those from shadow sizes and multiple photon ring measurements. Of particular interest is that these can be combined to separately measure γ:

$$\gamma = 2\pi \lim_{l\to\infty} l\frac{\omega_{I,l}}{\omega_{R,l}}. \tag{3.26}$$

While the above expressions invoke the high-l limit, in practice, for Kerr spacetime viewed by a polar observer and Schwarzschild spacetime, which were the cases of study in chapter 2 and 3, the approximations are good to better than 5% by $l = 2$,improving rapidly thereafter [11](see Figure 3.5). Of course, this does not confer any guarantees for alternative spacetimes. Nevertheless, for illustrative purposes we consider the implications of the LIGO QNM measurements. However, it is worth mentioning that by considering a polar observer, which implies $L_z = 0$, it immediately follows that $m = 0$ for the Quasinormal Modes. Thus, in Figure Figure 3.5, we exclusively focus on different values of l with $m = 0$. However, we also show the corresponding region between $m = \pm 2$ for $l = 2$ to provide a visual representation of the deviation across various quantum numbers.

Gravitational Wave Inspiral

EMRIs have the significant virtue of the secondary being a perturbation on the spacetime of the much more massive primary [5]. Therefore, as with QMNs, the dynamics of the

[3]Since we are considering the case with $L_z = 0$, equation II-21 in [89] reduces to I-1 in the same work, which is the expression that we used here.

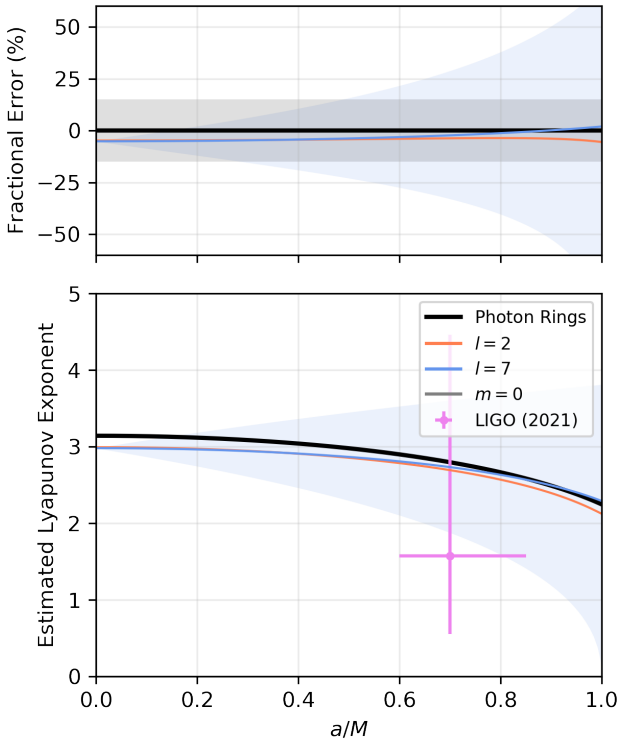

Figure 3.5: Bottom: polar-orbit Lyapunov exponent from (3.21) (black) in comparison to the estimates from the fundamental ($n = 0$) quasinormal modes, $2\pi l\Im(\omega_{lmn})/\Re(\omega_{lmn})$ for various l and m as tabulated by [11]. The range of values for $l = 7$ encompassed by $|m| \leq l$ is shaded in blue, with those for $m = -1, -2$ and $m = 0, 1, 2$ shown by the thin and thick lines, respectively, for $l = 2, 7$. For reference, the implied estimates from [2] are shown in magenta (error bars indicate 90% $4\pi\omega_I/\omega_R$ and final spin ranges). Top: the fractional difference between the QNM estimates and the polar-orbit Lyapunov exponent. The grey band shows the 15% region, similar to those expected for high S/N LIGO events [58].

EMRI system can be analyzed within the context of a stationary background spacetime, subject to the caveat regarding the dynamical sector of the underlying gravity theory. However, there is an additional complication: the inspiral typically occurs at $r > r_\gamma$.

A short discussion of the circular orbits of massive paricles in arbitrary spherically symmetric spacetimes may be found in Appendix E. An implicit expression for the radius of the ISCO, which terminates the inspiral regime, is given in Equation E.8. While it is clear that the detection of a photon ring ensures that stable circular orbits do not exist a r_γ (see Appendix E), general statements about the ordering and proxmity of the ISCO and photon orbit depend on the particular form of $N(r)$. As a result, some assumption regarding the extrapolation of $N(r)$ away from r_γ is necessary to make any estimate of the implications of inspiral waveform measurements for deviations from general relativity.

Chapter 4

Conclusion

The EHT images of M87* and Sgr A* provide a new, direct window into the properties of astrophysical black holes. Shadow size measurements, and more generally, measurements of the size of photon rings, provide a means to directly probe the spacetime geometry of black holes. However, interpreting the gravitational implications of these measurements requires some care due to the nonlinear nature of general relativity near black hole event horizons and limited information contained in a single (or handful) of size measurements.

Significant qualitative conclusions may be reached already based solely upon the detection of various image features. The detection of a shadow immediately implies that $N'(r_\gamma) > 0$. The detection of any photon ring implies that $N''(r_\gamma) < 0$. These hold independent of the shadow or photon ring size.

The size of the shadow is directly related to $N'(r_\gamma)$ (at least for the cases where the inclination is almost zero): measuring the shadow size is synonymous with measuring the radial derivative of the tt-component of the metric in areal coordinates. In this sense, precise shadow size measurements generate precise metric constraints. However, there is no constraint on $N(r_\gamma)$ from the shadow size alone, and thus shadow size measurements by themselves do not provide any limit on the magnitude of a putative deviation in the tt-component of the metric. In this sense, precise shadow measurements are uninformative.

Shadow measurements do not offer any insights into the various arbitrary functions of the general metric, such as $F(r)$, $B(r)$, or $f(r)$, as well. Similarly, both shadow measurements and multiple photon ring measurements fail to provide information about the ergosphere's location and properties since these can only be established through $F^2(r)$. Furthermore, solely relying on shadow measurements does not provide any details about the radial distances, which can be determined by the g_{rr} and consequently $B^2(r)$.

When translated to spacetime parameters, either via parameterized metric expansions or explicit alternative spacetimes, precise shadow size measurements can appear to impose strong constraints on both $N(r_\gamma)$ and $N'(r_\gamma)$. The constraint on $N(r_\gamma)$ is a direct consequence of the prior that has been adopted via the choice of the underlying metric. In the case of parameterized metric expansions, for which there is little significance to this prior, the strength of the attendant limit on $N(r_\gamma)$ is illusory. Indeed, it is straightforward to generate examples of perturbed metrics that are otherwise consistent with all existing constraints for Sgr A* and M87*, including the recent EHT shadow sizes, that have nearly arbitrary magnitude metric perturbations at the photon orbit. Claims in the literature that shadow size measurements limit a specific metric expansion coefficient, or a linear combination of coefficients, must be understood within a narrow context for a similar reason.

Nevertheless, because shadow size measurements do impose a strong measurement on some facet of the underlying spacetime, we propose an alternative way to characterize their gravitational implications: the values of $N(r)$, $N'(r)$, $N''(r)/B^2(r)$, etc., measured at r_γ. This series has the virtue of being a nonparametric and nonperturbative description of the shadow size measurement — in spherical symmetry and some cases of axi-symmetry, which we explored in this work, the identifications are exact. However, they are complicated by the a priori unknown value of r_γ, i.e., properties of the metric are constrained at an important dynamical location in the spacetime whose location is otherwise unknown.

The proposed formalism in this study establishes a comprehensive framework for cross-correlating between various tests and measurements of near-horizon probes. One notable application of this framework involves gravitational wave measurements, specifically the assessment of Quasi-Normal Mode (QNM) frequencies in binary mergers and pulsars. To compare these measurements with shadow size measurements, we propose utilizing the connection between the critical photon curve (shadow) and the QNM frequency. This approach enables the combination of these two measurements, serving as a valuable tool for exploring gravity at near-horizon distances and imposing more stringent constraints on different theoretical frameworks. It is also worth mentioning that there are numerous other tests that can be probed using this general framework such as, redshift Measurements in relativistically broadened iron fuorescence lines [22, 82], Light Echos [69, 52], etc.

Despite the unknown r_γ, this proposal presents a particularly useful basis for comparing near-horizon measurements, including photon rings, shadow sizes, and black hole ringdowns, all of which are dominated by massless particle dynamics near the event horizon, and therefore the photon orbit. It is also convenient theoretically, providing a more natural quantity for theoretical comparison and obviating the need for full ray-tracing and radiative transfer simulations and/or mode spectrum computation.

This basis remains poorly connected to gravity measurements that probe very different spatial scales. This is a natural consequence of the afore-mentioned nonlinearity expected near the photon orbit: the unavoidable price of adopting a nonperturbative way to characterize near-horizon observations is difficulty in making comparisons to perturbative characterizations of other measurements. This complicates, e.g., quantitatively relating EHT shadow size measurements to solar system tests or observations of the inspiral phase of black hole mergers outside of a particular gravity theory.

We have focused on spherically symmetric spacetimes for simplicity in chapter 2. However, to linear order in spin, all of the results obtained for Schwarzschild continue to apply for polar observers (the relevant inclination for M87*). We also explored the expansion of the nonparametric, nonperturbative characterization to integrable rotating spacetimes with arbitrary spins in chapter 3. Nevertheless, even the simple cases explored here, elucidate the power and limitations of measurements of the shadow and photon ring sizes.

Although this study presents a fairly comprehensive framework, there is potential for further generalization. One of the assumptions made in this thesis, within the context of axi-symmetric spacetime, was the presence of a separable action. This assumption allows for the existence of a fourth constant of motion, ensuring the integrability of geodesics in this particular spacetime. Consequently, a future direction for this project involves extending the framework to incorporate a non-separable action and investigating non-integrable null rays. Additionally, in Chapter 3, a simplification was made by considering the viewpoint of polar observers. Expanding this perspective to encompass a more general observer's viewpoint would enhance the generality of the study and can be considered as another direction for the future work.

References

[1] R. Abbott, et al., and LIGO Scientific Collaboration. Observation of gravitational waves from a binary black hole merger. *Phys. Rev. Lett.*, 116:061102, Feb 2016.

[2] R. Abbott, et al., LIGO Scientific Collaboration, and Virgo Collaboration. Tests of general relativity with binary black holes from the second LIGO-Virgo gravitational-wave transient catalog. *Physical Review D*, 103(12):122002, June 2021.

[3] Pau Amaro-Seoane and et al. Laser Interferometer Space Antenna. *arXiv e-prints*, page arXiv:1702.00786, February 2017.

[4] Jay Armas, Yangyang Cai, Geoffrey Compère, David Garfinkle, and Samuel E. Gralla. Consistent Blandford-Znajek expansion. *Journal of Cosmology and Astroparticle Physics*, 2020(4):009, April 2020.

[5] Stanislav Babak, Jonathan Gair, Alberto Sesana, Enrico Barausse, Carlos F. Sopuerta, Christopher P. L. Berry, Emanuele Berti, Pau Amaro-Seoane, Antoine Petiteau, and Antoine Klein. Science with the space-based interferometer LISA. V. Extreme mass-ratio inspirals. *Physical Review D*, 95(10):103012, May 2017.

[6] Tessa Baker, Dimitrios Psaltis, and Constantinos Skordis. Linking Tests of Gravity on All Scales: from the Strong-field Regime to Cosmology. *Astrophysical Journal*, 802(1):63, March 2015.

[7] James M Bardeen. Non-singular general-relativistic gravitational collapse. In *Proc. Int. Conf. GR5, Tbilisi*, volume 174, page 174, 1968.

[8] Per Berglund, Jishnu Bhattacharyya, and David Mattingly. Mechanics of universal horizons. *Phys. Rev. D*, 85:124019, Jun 2012.

[9] Per Berglund, Jishnu Bhattacharyya, and David Mattingly. Mechanics of universal horizons. *Phys. Rev. D*, 85:124019, Jun 2012.

[10] Per Berglund, Jishnu Bhattacharyya, and David Mattingly. Mechanics of universal horizons. *Physical Review D*, 85(12):124019, June 2012.

[11] Emanuele Berti, Vitor Cardoso, and Andrei O. Starinets. TOPICAL REVIEW: Quasinormal modes of black holes and black branes. *Classical and Quantum Gravity*, 26(16):163001, August 2009.

[12] Roger Blandford and Noémie Globus. Ergomagnetosphere, ejection disc, magnetopause in M87 - I. Global flow of mass, angular momentum, energy, and current. *Monthly Notices of the RAS*, 514(4):5141–5158, August 2022.

[13] Avery E. Broderick and Abraham Loeb. Imaging optically-thin hotspots near the black hole horizon of Sgr A* at radio and near-infrared wavelengths. *Monthly Notices of the RAS*, 367(3):905–916, April 2006.

[14] Avery E. Broderick, Dominic W. Pesce, Roman Gold, Paul Tiede, Hung-Yi Pu, Richard Anantua, Silke Britzen, Chiara Ceccobello, Koushik Chatterjee, Yongjun Chen, Nicholas S. Conroy, Geoffrey B. Crew, Alejandro Cruz-Osorio, Yuzhu Cui, Sheperd S. Doeleman, Razieh Emami, Joseph Farah, Christian M. Fromm, Peter Galison, Boris Georgiev, Luis C. Ho, David J. James, Britton Jeter, Alejandra Jimenez-Rosales, Jun Yi Koay, Carsten Kramer, Thomas P. Krichbaum, Sang-Sung Lee, Michael Lindqvist, Iván Martí-Vidal, Karl M. Menten, Yosuke Mizuno, James M. Moran, Monika Moscibrodzka, Antonios Nathanail, Joey Neilsen, Chunchong Ni, Jongho Park, Vincent Piétu, Luciano Rezzolla, Angelo Ricarte, Bart Ripperda, Lijing Shao, Fumie Tazaki, Kenji Toma, Pablo Torne, Jonathan Weintroub, Maciek Wielgus, Feng Yuan, Shan-Shan Zhao, and Shuo Zhang. The Photon Ring in M87*. *Astrophysical Journal*, 935(1):61, August 2022.

[15] Avery E. Broderick, Dominic W. Pesce, Paul Tiede, Hung-Yi Pu, and Roman Gold. Hybrid Very Long Baseline Interferometry Imaging and Modeling with THEMIS. *Astrophysical Journal*, 898(1):9, July 2020.

[16] Avery E. Broderick, Paul Tiede, Dominic W. Pesce, and Roman Gold. Measuring Spin from Relative Photon-ring Sizes. *Astrophysical Journal*, 927(1):6, March 2022.

[17] K. A. Bronnikov. Regular magnetic black holes and monopoles from nonlinear electrodynamics. *Phys. Rev. D*, 63:044005, Jan 2001.

[18] Brandon Carter. Global Structure of the Kerr Family of Gravitational Fields. *Physical Review*, 174(5):1559–1571, October 1968.

[19] Roberto Casadio, Alessandro Fabbri, and Lorenzo Mazzacurati. New black holes in the brane world? *Phys. Rev. D*, 65:084040, Apr 2002.

[20] C. T. Cunningham and James M. Bardeen. The Optical Appearance of a Star Orbiting an Extreme Kerr Black Hole. *Astrophysical Journal*, 183:237–264, July 1973.

[21] C. T. Cunningham and James M. Bardeen. The Optical Appearance of a Star Orbiting an Extreme Kerr Black Hole. *Astrophysical Journal*, 183:237–264, July 1973.

[22] I. de La Calle Pérez, A. L. Longinotti, M. Guainazzi, S. Bianchi, M. Dovčiak, M. Cappi, G. Matt, G. Miniutti, P. O. Petrucci, E. Piconcelli, G. Ponti, D. Porquet, and M. Santos-Lleó. FERO: Finding extreme relativistic objects. I. Statistics of relativistic Fe K_α lines in radio-quiet Type 1 AGN. *Astronomy and Astrophysics*, 524:A50, December 2010.

[23] Tuan Do, Aurelien Hees, Andrea Ghez, Gregory D. Martinez, Devin S. Chu, Siyao Jia, Shoko Sakai, Jessica R. Lu, Abhimat K. Gautam, Kelly Kosmo O'Neil, Eric E. Becklin, Mark R. Morris, Keith Matthews, Shogo Nishiyama, Randy Campbell, Samantha Chappell, Zhuo Chen, Anna Ciurlo, Arezu Dehghanfar, Eulalia Gallego-Cano, Wolfgang E. Kerzendorf, James E. Lyke, Smadar Naoz, Hiromi Saida, Rainer Schödel, Masaaki Takahashi, Yohsuke Takamori, Gunther Witzel, and Peter Wizinowich. Relativistic redshift of the star S0-2 orbiting the Galactic Center supermassive black hole. *Science*, 365(6454):664–668, August 2019.

[24] Sheperd Doeleman, Eric Agol, Don Backer, Fred Baganoff, Geoffrey C. Bower, Avery Broderick, Andrew Fabian, Vincent Fish, Charles Gammie, Paul Ho, Mareki Honman, Thomas Krichbaum, Avi Loeb, Dan Marrone, Mark Reid, Alan Rogers, Irwin Shapiro, Peter Strittmatter, Remo Tilanus, Jonathan Weintroub, Alan Whitney, Melvyn Wright, and Lucy Ziurys. Imaging an Event Horizon: submm-VLBI of a Super Massive Black Hole. In *astro2010: The Astronomy and Astrophysics Decadal Survey*, volume 2010, page 68, January 2009.

[25] Sheperd Doeleman, Lindy Blackburn, Jason Dexter, Jose L. Gomez, Michael D. Johnson, Daniel C. Palumbo, Jonathan Weintroub, Joseph R. Farah, Vincent Fish, Laurent Loinard, Colin Lonsdale, Gopal Narayanan, Nimesh A. Patel, Dominic W. Pesce, Alexander Raymond, Remo Tilanus, Maciek Wielgus, Kazunori Akiyama, Geoffrey Bower, Avery Broderick, Roger Deane, Christian Michael Fromm, Charles Gammie, Roman Gold, Michael Janssen, Tomohisa Kawashima, Thomas Krichbaum, Daniel P. Marrone, Lynn D. Matthews, Yosuke Mizuno, Luciano Rezzolla, Freek Roelofs, Eduardo Ros, Tuomas K. Savolainen, Feng Yuan, Guangyao Zhao, Lindy Blackburn,

Sheperd Doeleman, Jason Dexter, Jose L. Gomez, Michael D. Johnson, Daniel C. Palumbo, Jonathan Weintroub, Joseph R. Farah, Vincent Fish, Laurent Loinard, Colin Lonsdale, Gopal Narayanan, Nimesh A. Patel, Dominic W. Pesce, Alexander Raymond, Remo Tilanus, Maciek Wielgus, Kazunori Akiyama, Geoffrey Bower, Avery Broderick, Roger Deane, Christian Michael Fromm, Charles Gammie, Roman Gold, Michael Janssen, Tomohisa Kawashima, Thomas Krichbaum, Daniel P. Marrone, Lynn D. Matthews, Yosuke Mizuno, Luciano Rezzolla, Freek Roelofs, Eduardo Ros, Tuomas K. Savolainen, Feng Yuan, and Guangyao Zhao. Studying Black Holes on Horizon Scales with VLBI Ground Arrays. In *Bulletin of the American Astronomical Society*, volume 51, page 256, September 2019.

[26] A. Einstein. Zur Elektrodynamik bewegter Körper. *Annalen der Physik*, 322(10):891–921, January 1905.

[27] A. Einstein. Erklarung der Perihelionbewegung der Merkur aus der allgemeinen Relativitatstheorie. *Sitzungsber. preuss.Akad. Wiss*, 47:831–839, January 1915.

[28] Albert Einstein. Approximative Integration of the Field Equations of Gravitation. *Sitzungsber. Preuss. Akad. Wiss. Berlin (Math. Phys.)*, 1916:688–696, 1916.

[29] Albert Einstein. HAMILTONsches Prinzip und allgemeine Relativitätstheorie. *Sitzungsberichte der Königlich Preussischen Akademie der Wissenschaften*, pages 1111–1116, January 1916.

[30] Event Horizon Telescope Collaboration et al. First M87 Event Horizon Telescope Results. I. The Shadow of the Supermassive Black Hole. *Astrophysical Journal l*, 875:L1, April 2019.

[31] Event Horizon Telescope Collaboration et al. First M87 Event Horizon Telescope Results. II. Array and Instrumentation. *Astrophysical Journal l*, 875:L2, April 2019.

[32] Event Horizon Telescope Collaboration et al. First M87 Event Horizon Telescope Results. III. Data Processing and Calibration. *Astrophysical Journal l*, 875:L3, April 2019.

[33] Event Horizon Telescope Collaboration et al. First M87 Event Horizon Telescope Results. IV. Imaging the Central Supermassive Black Hole. *Astrophysical Journal l*, 875:L4, April 2019.

[34] Event Horizon Telescope Collaboration et al. First M87 Event Horizon Telescope Results. V. Physical Origin of the Asymmetric Ring. *Astrophysical Journal l*, 875:L5, April 2019.

[35] Event Horizon Telescope Collaboration et al. First M87 Event Horizon Telescope Results. VI. The Shadow and Mass of the Central Black Hole. *Astrophysical Journal l*, 875:L6, April 2019.

[36] Event Horizon Telescope Collaboration et al. First Sagittarius A* Event Horizon Telescope Results. I. The Shadow of the Supermassive Black Hole in the Center of the Milky Way. *Astrophysical Journal l*, 930(2):L12, May 2022.

[37] Event Horizon Telescope Collaboration et al. First Sagittarius A* Event Horizon Telescope Results. II. EHT and Multiwavelength Observations, Data Processing, and Calibration. *Astrophysical Journal l*, 930(2):L13, May 2022.

[38] Event Horizon Telescope Collaboration et al. First Sagittarius A* Event Horizon Telescope Results. III. Imaging of the Galactic Center Supermassive Black Hole. *Astrophysical Journal l*, 930(2):L14, May 2022.

[39] Event Horizon Telescope Collaboration et al. First Sagittarius A* Event Horizon Telescope Results. IV. Variability, Morphology, and Black Hole Mass. *Astrophysical Journal l*, 930(2):L15, May 2022.

[40] Event Horizon Telescope Collaboration et al. First Sagittarius A* Event Horizon Telescope Results. V. Testing Astrophysical Models of the Galactic Center Black Hole. *Astrophysical Journal l*, 930(2):L16, May 2022.

[41] Event Horizon Telescope Collaboration et al. First Sagittarius A* Event Horizon Telescope Results. VI. Testing the Black Hole Metric. *Astrophysical Journal l*, 930(2):L17, May 2022.

[42] A. C. Fabian, M. J. Rees, L. Stella, and N. E. White. X-ray fluorescence from the inner disc in Cygnus X-1. *Monthly Notices of the RAS*, 238:729–736, May 1989.

[43] A. C. Fabian, S. Vaughan, K. Nandra, K. Iwasawa, D. R. Ballantyne, J. C. Lee, A. De Rosa, A. Turner, and A. J. Young. A long hard look at MCG-6-30-15 with XMM-Newton. *Monthly Notices of the RAS*, 335(1):L1–L5, September 2002.

[44] Valeri P. Frolov. Notes on nonsingular models of black holes. *Phys. Rev. D*, 94:104056, Nov 2016.

[45] Jonathan Gair and Nicolás Yunes. Approximate waveforms for extreme-mass-ratio inspirals in modified gravity spacetimes. *Physical Review D*, 84(6):064016, September 2011.

[46] Alberto García, Dmitri Galtsov, and Oleg Kechkin. Class of stationary axisymmetric solutions of the einstein-maxwell-dilaton-axion field equations. *Phys. Rev. Lett.*, 74:1276–1279, Feb 1995.

[47] David Garfinkle, Gary T. Horowitz, and Andrew Strominger. Charged black holes in string theory. *Phys. Rev. D*, 43:3140–3143, May 1991.

[48] Karl Gebhardt, Joshua Adams, Douglas Richstone, Tod R. Lauer, S. M. Faber, Kayhan Gültekin, Jeremy Murphy, and Scott Tremaine. The Black Hole Mass in M87 from Gemini/NIFS Adaptive Optics Observations. *Astrophysical Journal*, 729(2):119, March 2011.

[49] Samuel E. Gralla, Daniel E. Holz, and Robert M. Wald. Black hole shadows, photon rings, and lensing rings. *Physical Review D*, 100(2):024018, July 2019.

[50] GRAVITY Collaboration, R. Abuter, N. Aimar, A. Amorim, J. Ball, M. Bauböck, J. P. Berger, H. Bonnet, G. Bourdarot, W. Brandner, V. Cardoso, Y. Clénet, Y. Dallilar, R. Davies, P. T. de Zeeuw, J. Dexter, A. Drescher, F. Eisenhauer, N. M. Förster Schreiber, A. Foschi, P. Garcia, F. Gao, E. Gendron, R. Genzel, S. Gillessen, M. Habibi, X. Haubois, G. Heißel, T. Henning, S. Hippler, M. Horrobin, L. Jochum, L. Jocou, A. Kaufer, P. Kervella, S. Lacour, V. Lapeyrère, J. B. Le Bouquin, P. Léna, D. Lutz, T. Ott, T. Paumard, K. Perraut, G. Perrin, O. Pfuhl, S. Rabien, J. Shangguan, T. Shimizu, S. Scheithauer, J. Stadler, A. W. Stephens, O. Straub, C. Straubmeier, E. Sturm, L. J. Tacconi, K. R. W. Tristram, F. Vincent, S. von Fellenberg, F. Widmann, E. Wieprecht, E. Wiezorrek, J. Woillez, S. Yazici, and A. Young. Mass distribution in the Galactic Center based on interferometric astrometry of multiple stellar orbits. *Astronomy and Astrophysics*, 657:L12, January 2022.

[51] Margherita Grespan and Marek Biesiada. Strong Gravitational Lensing of Gravitational Waves: A Review. *Universe*, 9(5):200, April 2023.

[52] Shahar Hadar, Michael D. Johnson, Alexandru Lupsasca, and George N. Wong. Photon ring autocorrelations. *Physical Review D*, 103(10), may 2021.

[53] Sean A. Hayward. Formation and evaporation of nonsingular black holes. *Phys. Rev. Lett.*, 96:031103, Jan 2006.

[54] David Hilbert. Nachrichten von der königlichen gesellschaft der wissenschaften zu göttingen—mathematisch-physikalische klasse, chapter die grundlagen der physik—zweite mitteilung. *Weidmannsche Buchhandlung, Berlin*, pages 53–76, 1917.

[55] G. Hobbs, A. Archibald, Z. Arzoumanian, D. Backer, M. Bailes, N. D. R. Bhat, M. Burgay, S. Burke-Spolaor, D. Champion, I. Cognard, W. Coles, J. Cordes, P. Demorest, G. Desvignes, R. D. Ferdman, L. Finn, P. Freire, M. Gonzalez, J. Hessels, A. Hotan, G. Janssen, F. Jenet, A. Jessner, C. Jordan, V. Kaspi, M. Kramer, V. Kondratiev, J. Lazio, K. Lazaridis, K. J. Lee, Y. Levin, A. Lommen, D. Lorimer, R. Lynch, A. Lyne, R. Manchester, M. McLaughlin, D. Nice, S. Oslowski, M. Pilia, A. Possenti, M. Purver, S. Ransom, J. Reynolds, S. Sanidas, J. Sarkissian, A. Sesana, R. Shannon, X. Siemens, I. Stairs, B. Stappers, D. Stinebring, G. Theureau, R. van Haasteren, W. van Straten, J. P. W. Verbiest, D. R. B. Yardley, and X. P. You. The International Pulsar Timing Array project: using pulsars as a gravitational wave detector. *Classical and Quantum Gravity*, 27(8):084013, April 2010.

[56] G. B. Hobbs, R. T. Edwards, and R. N. Manchester. TEMPO2, a new pulsar-timing package - I. An overview. *Monthly Notices of the RAS*, 369(2):655–672, June 2006.

[57] R. A. Hulse and J. H. Taylor. Discovery of a pulsar in a binary system. *Astrophysical Journal, Letters*, 195:L51–L53, January 1975.

[58] Maximiliano Isi and Will M. Farr. Analyzing black-hole ringdowns. *arXiv e-prints*, page arXiv:2107.05609, July 2021.

[59] Stanley L. Jaki. Johann Georg von Soldner and the gravitational bending of light, with an English translation of his essay on it published in 1801. *Foundations of Physics*, 8(11-12):927–950, December 1978.

[60] Tim Johannsen. Regular black hole metric with three constants of motion. *Physical Review D*, 88(4):044002, August 2013.

[61] Michael D. Johnson, Alexandru Lupsasca, Andrew Strominger, George N. Wong, Shahar Hadar, Daniel Kapec, Ramesh Narayan, Andrew Chael, Charles F. Gammie, Peter Galison, Daniel C. M. Palumbo, Sheperd S. Doeleman, Lindy Blackburn, Maciek Wielgus, Dominic W. Pesce, Joseph R. Farah, and James M. Moran. Universal interferometric signatures of a black hole's photon ring. *Science Advances*, 6(12):eaaz1310, March 2020.

[62] Kimet Jusufi. Quasinormal modes of black holes surrounded by dark matter and their connection with the shadow radius. *Phys. Rev. D*, 101:084055, Apr 2020.

[63] D. I. Kazakov and S. N. Solodukhin. On quantum deformation of the Schwarzschild solution. *Nuclear Physics B*, 429(1):153–176, October 1994.

[64] Prashant Kocherlakota, et al., and EHT Collaboration. Constraints on black-hole charges with the 2017 EHT observations of M87*. *Physical Review D*, 103(10):104047, May 2021.

[65] Prashant Kocherlakota and Luciano Rezzolla. Accurate mapping of spherically symmetric black holes in a parametrized framework. *Physical Review D*, 102(6):064058, September 2020.

[66] Prashant Kocherlakota, Luciano Rezzolla, et al. Private communication., 2021.

[67] M. Kramer, D. R. Lorimer, A. G. Lyne, M. McLaughlin, M. Burgay, N. D'Amico, A. Possenti, F. Camilo, P. C. C. Freire, B. C. Joshi, R. N. Manchester, J. Reynolds, J. Sarkissian Australia Telescope National Facility, Csiro, Australia I. H. Stairs, and R. D. Ferdman. Testing GR with the Double Pulsar: Recent Results. In *22nd Texas Symposium on Relativistic Astrophysics*, pages 142–148, January 2005.

[68] M. Kramer, I. H. Stairs, R. N. Manchester, M. A. McLaughlin, A. G. Lyne, R. D. Ferdman, M. Burgay, D. R. Lorimer, A. Possenti, N. D'Amico, J. M. Sarkissian, G. B. Hobbs, J. E. Reynolds, P. C. C. Freire, and F. Camilo. Tests of General Relativity from Timing the Double Pulsar. *Science*, 314(5796):97–102, October 2006.

[69] Kotaro Moriyama, Shin Mineshige, Mareki Honma, and Kazunori Akiyama. Black Hole Spin Measurement Based on Time-domain VLBI Observations of Infalling Gas Clouds. *Astrophysical Journal*, 887(2):227, December 2019.

[70] Ashish Narang, Subhendra Mohanty, and Abhass Kumar. Test of Kerr-Sen metric with black hole observations. *arXiv e-prints*, page arXiv:2002.12786, February 2020.

[71] Ramesh Narayan, Aleksander SÄ dowski, Robert F. Penna, and Akshay K. Kulkarni. GRMHD simulations of magnetized advection-dominated accretion on a non-spinning black hole: role of outflows. *Monthly Notices of the RAS*, 426(4):3241–3259, November 2012.

[72] E. T. Newman, E. Couch, K. Chinnapared, A. Exton, A. Prakash, and R. Torrence. Metric of a Rotating, Charged Mass. *Journal of Mathematical Physics*, 6(6):918–919, June 1965.

[73] Emmy Noether. Invariant Variation Problems. *Nachr. D. KÃnig. Gesellsch. D. Wiss. Zu GÃttingen*, pages 235–237, January 1918.

[74] R. Penrose and R. M. Floyd. Extraction of Rotational Energy from a Black Hole. *Nature Physical Science*, 229(6):177–179, February 1971.

[75] Oliver Porth, et al., and Event Horizon Telescope Collaboration. The Event Horizon General Relativistic Magnetohydrodynamic Code Comparison Project. *Astrophysical Journal s*, 243(2):26, August 2019.

[76] Dimitrios Psaltis, et al., and EHT Collaboration. Gravitational Test beyond the First Post-Newtonian Order with the Shadow of the M87 Black Hole. *PhRvL*, 125(14):141104, October 2020.

[77] H. Reissner. Über die eigengravitation des elektrischen feldes nach der einsteinschen theorie. *Annalen der Physik*, 355(9):106–120, 1916.

[78] Christopher S. Reynolds and Mitchell C. Begelman. Iron Fluorescence from within the Innermost Stable Orbit of Black Hole Accretion Disks. *Astrophysical Journal*, 488(1):109–118, October 1997.

[79] Luciano Rezzolla and Alexander Zhidenko. New parametrization for spherically symmetric black holes in metric theories of gravity. *Physical Review D*, 90(8):084009, October 2014.

[80] Domingos S. L. Soares. Newtonian gravitational deflection of light revisited. *arXiv e-prints*, page physics/0508030, August 2005.

[81] Ivan Zh. Stefanov, Stoytcho S. Yazadjiev, and Galin G. Gyulchev. Connection between black-hole quasinormal modes and lensing in the strong deflection limit. *Physical Review Letters*, 104(25), jun 2010.

[82] Y. Tanaka, K. Nandra, A. C. Fabian, H. Inoue, C. Otani, T. Dotani, K. Hayashida, K. Iwasawa, T. Kii, H. Kunieda, F. Makino, and M. Matsuoka. Gravitationally redshifted emission implying an accretion disk and massive black hole in the active galaxy MCG-6-30-15. *Nature*, 375(6533):659–661, June 1995.

[83] Sarah Vigeland, Nicolás Yunes, and Leo C. Stein. Bumpy black holes in alternative theories of gravity. *Physical Review D*, 83(10):104027, May 2011.

[84] Sebastian H. Völkel, Enrico Barausse, Nicola Franchini, and Avery E. Broderick. EHT tests of the strong-field regime of general relativity. *Classical and Quantum Gravity*, 38(21):21LT01, November 2021.

[85] Robert M. Wald. *General Relativity*. University of Chicago Press, 1984.

[86] Clifford M. Will. The Confrontation between General Relativity and Experiment. *Living Reviews in Relativity*, 17(1):4, December 2014.

[87] Hiroki Yajima and Takashi Tamaki. Black hole solutions in euler-heisenberg theory. *Phys. Rev. D*, 63:064007, Feb 2001.

[88] Hiroki Yajima and Takashi Tamaki. Black hole solutions in Euler-Heisenberg theory. *Physical Review D*, 63(6):064007, March 2001.

[89] Huan Yang. Relating black hole shadow to quasinormal modes for rotating black holes. *Physical Review D*, 103(8):084010, April 2021.

APPENDICES

Appendix A

Critical photon orbit for Schwarzschild space time

Due to the fact that Schwarzschild metric is static and spherically symmetrical, this space time has three integrals of motion. Thanks to Noether theorem any symmetry is associated with a conserved charge [73]. In the case of this space-time, spherical symmetry leads to the constancy of three quantities. We choose these to be the angular momentum along the polar axis, the total angular momentum and energy, namely L_z, L, and E respectively. Therefore, the value of energy can be expressed as,

$$E = p_t = g_{tt}\dot{t} \tag{A.1}$$

Where $\dot{f}$ means $df/d\lambda$, also angular momentum in z direction is,

$$L_z = p_\phi = g_{\phi\phi}p^\phi, \tag{A.2}$$

and $p_\phi = \dot{\phi}$. Inserting these equations for null rays, which basically means $ds^2 = 0$, in Schwartzshild metric which results in,

$$0 = -\frac{E^2}{f(r)} + \frac{\dot{r}^2}{f(r)} + r^2\dot{\theta}^2 + \frac{L_z^2}{r^2\sin^2\theta}, \tag{A.3}$$

which $f(r) = 1-2M/r$. Due to the spherically symmetry the spatial part of the trajectories lives in a 2D plane thus, we can set $\theta = \pi/2$ and $\dot{\theta} = 0$, without loss of generality. Therefore, (A.3) reduces to,

$$\dot{r}^2 = E^2 - f(r)\frac{L_z^2}{r^2}. \tag{A.4}$$

Since $g_{tt} = -f(r)$, we can define an effective potential by,

$$V_{\text{eff}}(r) = -g_{tt}\frac{L_z^2}{r^2}. \tag{A.5}$$

In terms of which we obtain,

$$\dot{r}^2 + V_{\text{eff}}(r) = E^2. \tag{A.6}$$

Figure A.1 helps identifying the location and existence of the turning points, where are the points that $\dot{r} = 0$ or equivalently $V_{\text{eff}}(r) = E^2$. Therefore, one can see the extermal point

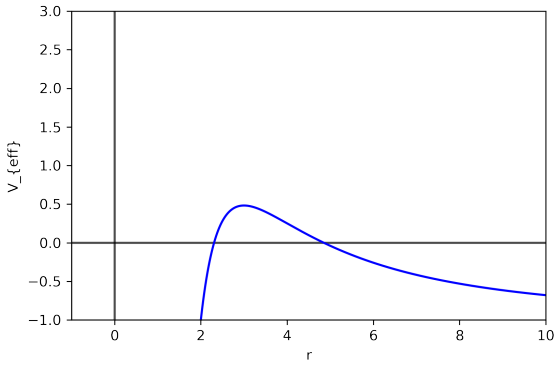

Figure A.1: The effective potential for null geodesics in the Schwarzschild spacetime as a function of areal radius. The black horizontal line shows the $V_{\text{eff}} = 0$ and the curve represent a null ray with $L_z = \sqrt{40}$.

of this curve could be equal to 0 for ,

$$\left(\frac{L_z}{E}\right)^2 = \frac{r^2}{-g_{tt}(r)} \tag{A.7}$$

On the other hand, by taking time derivative from (A.6) we get,

$$\ddot{r} = \frac{1}{2}V'_{\text{eff}}(r), \tag{A.8}$$

where V'_{eff} is the radial derivative of V_{eff}, solving these two equations simultaneously we get the critical photon orbit,

$$r_\gamma = \frac{2g_{tt}(r_\gamma)}{g'_{tt}(r_\gamma)}, \tag{A.9}$$

which is the radius of photon circular orbit. The value for r_γ and the critical impact parameter for the Schwarzschild metric are equal to,

$$r_\gamma = 3M \quad \text{and} \quad \left(\frac{L_z}{E}\right) = \sqrt{27}. \tag{A.10}$$

According to the predictions of general relativity, the null photon circle is not stable. We will elaborate on the reason for this instability in the following. However, before explaining that we need to discuss about impact parameter of null rays.

Photons coming from infinity with a impact parameter b and angular momentum L_z follow this equation,

$$L_z = r \times p, \tag{A.11}$$

also one can see, since $p = r\dot{\phi}$,

$$\dot{\phi} = \frac{L_z}{r^2} \tag{A.12}$$

Additionally, one can deduce at infinity,

$$L_z = b|p|. \tag{A.13}$$

For the null rays in natural units we know $p = E$. Therefore,

$$L_z = bE \tag{A.14}$$

Which b, the impact parameter, is defined as the perpendicular distance between the path of a projectile and the black hole at infinity.

Now by using equations (A.9) and (A.7) we have,

$$b_\gamma = \frac{r_\gamma}{g_{tt}(r_\gamma)} = \sqrt{27}. \tag{A.15}$$

This impact parameter determines the shadow size that can be observed on the black hole Images [35, 41].

Appendix B

Multiple Photon Rings in Schwarzschild spacetime

Consider a null ray positioned immediately outside the photon circular orbit at $r_\gamma + \delta r_0$, with an impact parameter slightly greater than the critical impact parameter $b_\gamma + \delta b$. This null ray starts from $r+\delta r_0$ and proceed to $r(t) = r_\gamma + \delta r(t)$. Here, $|\delta r| << r_\gamma$ and $\delta b << b_\gamma$. Using the Taylor expansion around r_γ to describe this ray gives,

$$\ddot{r}(r_\gamma + \delta r) = \ddot{r}(r_\gamma) + \ddot{r}'(r_\gamma)\delta r \tag{B.1}$$

where $\ddot{r}(r_\gamma)$ is equal to zero due to definition of circular orbit and $\ddot{r}'(r_\gamma)$ is radial partial derivative of $\ddot{r}(r_\gamma)$ at the photon orbit. For the Schwarzschild metric this is equal to,

$$\ddot{r}'|_{r_\gamma} = \frac{1}{2}\,\frac{g_{tt}(r_\gamma)}{r_\gamma^2 g_{rr}(r_\gamma)}\left(\frac{r^2}{g_{tt}}\right)''\Bigg|_{r_\gamma}. \tag{B.2}$$

Solving (B.2), gets,

$$\delta r = \delta r_0 e^{\omega\tau} \tag{B.3}$$

where ω is,

$$\omega^2 = \frac{1}{2}\frac{g_{tt}(r_\gamma)}{r_\gamma^2 g_{rr}(r_\gamma)}\left(\frac{r^2}{g_{tt}}\right)''|_{r_\gamma}, \tag{B.4}$$

and for Schwarzschild it is equal to $\frac{1}{\sqrt{27}}$. As a result, it can be inferred that the photon orbit at r_γ is unstable and the null rays slightly outside the r_γ circulate around the black hole a finite amount of times before reaching a point where the Taylor expansion becomes

invalid (r=R), after which they continue on their unbound trajectories towards infinity. Furthermore, it is noteworthy to mention that the equation (B.3) also indicates that null rays within r_γ, ($\delta r < 0$) exhibit an exponential fall into the black hole, which in turn predicts the presence of a dark region the in black hole images. In order to see that we need to check the ϕ component of the trajectory. Starting from defining the Lyapunov exponent, γ, as,

$$\pi \frac{d\delta r}{d\phi} = \gamma \delta r \tag{B.5}$$

and using (B.3),(A.12) and (A.15) one can conclude [1],

$$\frac{d\delta r}{d\phi} = \frac{d\delta r}{d\tau}\frac{d\tau}{d\phi} = \omega \left(\frac{r_\gamma^2}{b_\gamma}\right) \delta r \rightarrow \gamma = \pi \left(\frac{r_\gamma}{b_\gamma}\right) \sqrt{\frac{1}{2}\frac{g_{tt}(r_\gamma)}{g_{rr}(r_\gamma)} \left(\frac{r^2}{g_{tt}}\right)''|_{r_\gamma}} \tag{B.6}$$

Thus,

$$\delta r = \delta r_0 e^{\gamma\phi/\pi}, \tag{B.7}$$

where the Schwarzschild value of γ predicted by GR is π. Moreover, by assuming that the Taylor expansion fails at a particular radius ($\delta r = R_n$), where the photon completes n revolutions around the black hole ($\phi = \pi n$), we can derive the following,

$$R_n = \delta r_0 e^{\gamma n}. \tag{B.8}$$

This results in,

$$n = \frac{1}{\gamma} \ln \frac{R_n}{\delta r_0}. \tag{B.9}$$

These photons can get arbitrarily close to the photon circle, i.e., δr_0 can get arbitrarily close to zero, thus due to (B.9), n can get arbitrarily big. Therefore we can see that GR predicts the shadow is bounded by an infinite number of these subsequent rings which are the effect of strong gravitational lensing at the vicinity of the black hole horizon. These photon rings represent higher-order images of the photons emitted mainly from the accretion flow, which are heavily lensed as they pass by the black hole.

[1] I set $E = 1$ since energy is a constant of motion and can be rescaled to 1.

Appendix C

Critical photon orbit in Kerr space time

According to the No hair theorem, black holes can be uniquely characterized by their mass, spin, and charge. Since electromagnetism is significantly stronger than gravity, it is widely believed that black holes in nature are typically neutral, meaning that their mass and spin are sufficient to describe them. Additionally, the Birkhoff theorem states that the solution for axi-symmetric and stationary vacuum space-time in general relativity is unique, and it is known as the Kerr space-time. Therefore, General relativity predicts that the space-time surrounding all natural black holes can be described by the Kerr metric.

Now by using Kerr metric in Boyer-Lindquist coordinates,

$$ds^2 = -\left(1 - \frac{2Mr}{\Sigma}\right) dt^2 + \frac{\Sigma}{\Delta} dr^2 + \Sigma d\theta^2 + \left(r^2 + a^2 + \frac{2Mra^2}{\Sigma} \sin^2\theta\right) \sin^2\theta d\phi^2 - 2\left(\frac{2Mra\sin^2\theta}{\Sigma}\right) dt d\phi \quad \text{(C.1)}$$

where

$$\Sigma = r^2 + a^2 cos^2\theta \quad \text{and} \quad \Delta = r^2 - 2Mr + a^2. \quad \text{(C.2)}$$

Moreover due to the symmetries of this spacetime, it contains 3 constants of motion, which we explain in the following.

1. ∂_t is a Killing vector for this space time, thus,

$$E = p_t \quad \text{(C.3)}$$

energy is an integral of motion here.

2. ∂_ϕ is a Killing vector for this space time, thus,

$$L_z = p_\phi \tag{C.4}$$

angular momentum along the spinning axis (z-axis) is another integral of motion for this space time.

3. The Kerr metric has an additional non-trivial integral of motion which is called the Carter constant,

$$Q = p_\theta^2 + \cos^2\theta \left(a^2(\mu^2 - E^2) + (\frac{L_z}{\sin\theta})^2 \right) \tag{C.5}$$

where p_θ is the angular momentum in θ direction and μ is the particle's rest mass [18].

Particle's rest mass along with these integrals of motion guarantee that geodesics are integrable in this spacetime.

Since the action in this spacetime is separable [18], the equation for the radial position can be derived using the Hamiltonian-Jacobi method,

$$\dot{r}^2 = \frac{R(r)}{\Sigma^2}, \tag{C.6}$$

where $R(r)$ is,

$$R(r) = E^2[r^4 + (a^2 - \lambda^2 - q^2)r^2 - a^2q^2 + 2M\left((a-\lambda)^2 + q^2\right)r] \tag{C.7}$$

where M is the black hole's mass and ,

$$\lambda = \frac{L_z}{E} \quad \text{and} \quad q^2 = \frac{Q}{E^2} \tag{C.8}$$

Similar to the Schwarzschild black holes, we begin by finding the turning point, the place where

$$\dot{r} = 0 \rightarrow R(r) = 0 \tag{C.9}$$

Photons coming from specific impact parameters reach to the turning point. However, in this spacetime, impact parameters are more complex on the celestial sphere of a distant observer than they are in Schwarzschild spacetime. Figure C.1 illustrates this, where the

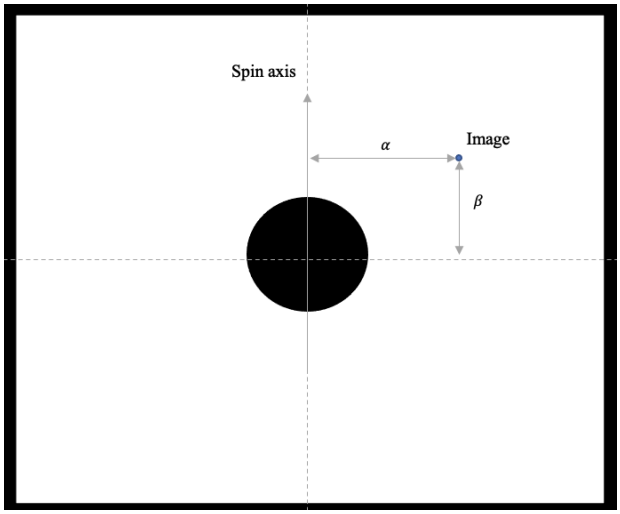

Figure C.1: Impact Parameter
impact parameter for a null ray coming from infinity in Kerr space time. The dotted line is the projection of axis of rotation on distance observer's screen

axis of rotation of the black hole is represnted by an arrow. α is the perpendicular impact parameter to the rotation axis, and β is the parallel impact parameter. The total value for the impact parameter is equal to, $b^2 = \beta^2 + a^2$.

To simplify matters, let us assume that the observer is viewing the black hole along the axis of rotation. Therefore the photon reaches the detectors at $\theta_0 = 0$ which by using equation 28 in [21] we derive,

$$\lambda = \alpha = 0 \tag{C.10}$$

and

$$\beta = E^2\sqrt{q^2 + a^2} \tag{C.11}$$

Now by using this and rewriting equation(C.7) one can get,

$$R = E^2(r^2 + a^2)^2\left(1 - \frac{\Delta}{(r^2 + a^2)^2}\beta^2\right) \tag{C.12}$$

therefore,

$$\dot{r}^2 = E^2\frac{1}{\Sigma^2}\left(1 - \frac{\Delta}{(r^2 + a^2)^2}\beta^2\right) \tag{C.13}$$

which is very similar to the effective potential that we found in (A.6) for non-spninng black holes in GR. In fact if we set a=0 we get,

$$\dot{r}^2 = E^2 \left(1 - f(r)\frac{q^2}{r^2}\right) \tag{C.14}$$

The expression is quite similar to (A.4), with the only distinction being that in the former case, we were examining null paths on the equatorial plane, whereas here, we are studying photons with $\theta_0 = 0$. Moreover, this is related to the fact that Schwarzschild space time also has Carter constant as an integral of motion and it is equal to setting $a = 0$ in (C.5), which gives,

$$Q = p_\theta^2 + \cos^2\theta \left(\frac{L_z^2}{\sin^2\theta}\right) \tag{C.15}$$

Now by setting $L_z = 0$ we get,

$$Q = p_\theta^2 \tag{C.16}$$

By inserting these in (A.3) we derive,

$$0 = \frac{E^2}{f(r)} + \frac{\dot{r}^2}{f(r)} + \frac{p_\theta^2}{r^2} \tag{C.17}$$

Therefore,

$$\dot{r}^2 = E^2 \left(1 - f(r)\frac{q^2}{r^2}\right) \tag{C.18}$$

which is compatible with (C.14). Having established that the previous calculations align with the Schwarzschild spacetime in the absence of spin, we can proceed with determining the radius of the photon orbit for null trajectories in Kerr spacetime with $\theta_0 = 0$, utilizing (C.13) and deriving $\dot{r}$ and $\ddot{r}$ we get,

$$\begin{aligned} r_\gamma &= M + 2M\sqrt{1 - \frac{a^2}{3M}}\cos\left[\frac{1}{3}\cos^{-1}\left(\frac{1 - a^2/M^2}{(1 - a^2/3M)^{3/2}}\right)\right]. \\ \beta^2 &= \frac{(r_\gamma^2 + a^2)^2}{\Delta(r_\gamma)} \end{aligned} \tag{C.19}$$

which is compatible with the results we saw in the Schwarzschild space time in the slow rotating regime.

Nevertheless, it is worthwhile to consider the general scenario where null rays may not necessarily have $\theta_0 = 0$. To determine the critical circular orbit for these trajectories, Equation (C.7) must be taken into account. The first step is to identify the constant radius orbit by finding the point where $\dot{r} = 0$,

$$\dot{r} = 0 \rightarrow R(r_\gamma) = 0 \tag{C.20}$$

To remain on this orbit, we need to ensure that $\ddot{r} = 0$,

$$\ddot{r} = 0 \rightarrow R'(r_\gamma) = 0 \tag{C.21}$$

Which in principle, we can solve for two out of the three quantities, r_γ, λ, and q, as a function of one of them. Furthermore, we can explore the subsequent photon rings in axi-symmetric space time by taking the similar path to the one that we took for spherically symmetric spacetimes before.

Appendix D

Multiple photon rings in Kerr Spacetime

Null rays coming from slightly different impact parameters create the subsequent photon rings that we review here, by starting from Taylor expanding $\ddot{r}$ around r_γ we get,

$$\ddot{r}(r_\gamma + \delta r_0) = \ddot{r}(r_\gamma) + \ddot{r}'(r_\gamma)\delta r_0, \tag{D.1}$$

where $\ddot{r}(r_\gamma)$ is equal to zero due to the definition of circular orbit and $\ddot{r}'(r_\gamma)$ is the radial partial derivative of $\ddot{r}(r_\gamma)$ at the photon orbit. Thus for a general observer this can be derived as,

$$\ddot{r}'(r_\gamma) = \frac{1}{2}\frac{1}{\Sigma\Delta g_{rr}}R''(r_\gamma), \tag{D.2}$$

where

$$\delta r = \delta r_0 e^{\omega\tau}. \tag{D.3}$$

By using (D.1) we see,

$$\omega^2 = \ddot{r}'(r_\gamma). \tag{D.4}$$

Also setting $L_z = 0$,

$$\omega^2 = \frac{E^2}{2}\frac{(r_\gamma^2 + a^2)^2}{\Sigma(r_\gamma)\Delta(r_\gamma)g_{rr}(r_\gamma)}\left[\frac{\Delta}{(r^2+a^2)^2}\right]''_{r_\gamma}\beta_\gamma^2 \tag{D.5}$$

This outcome is akin to (B.4) and precisely reduces to the calculations in the Schwarzschild spacetime, when a approaches zero.

We can proceed by introducing the Lyapunov exponent as we did for the Swartzshild space time but we will leave this part for chapter 3, where we can discuss this in more detail.

Moreover, to witness a shadow of the black hole, there should be a significant decline in brightness within the radius of the photon circle, leading to,

$$\ddot{r}'(r_\gamma) > 0 \tag{D.6}$$

which basically means if δr_0 is positive then this null ray exponentially gets further and further away and eventually escapes to infinity and reaches the detectors. Also if δr_0 is negative it will exponentially fall towards the black hole which results in exponentially decreasing of the brightness inside the photon circular orbit.

Appendix E

Circular Orbits of Massive Particles

General expressions for circular orbits for massive particles may be constructed for the family of space times described by the metric that been mentioned in chapter2 in a fashion similar to that used to obtain r_γ. We again require $\dot{r}$ and $\ddot{r}$ vanish. The first condition gives

$$\dot{r}^2 = \frac{1}{B^2(r)}\left[E^2 - N^2 - \frac{N^2}{r^2}L^2\right] = 0, \tag{E.1}$$

where $E = -u_t$ and $L = u_\phi$ are the conserved specific energy and specific angular momentum. From this, the second gives

$$\ddot{r} = \frac{N(r)}{B^2(r)}\left[N'(r) + L^2\left(\frac{N'(r)}{r^2} - \frac{N(r)}{r^3}\right)\right] = 0, \tag{E.2}$$

where we employed the previous condition. Together, these imply that for circular orbits,

$$L \equiv u_\phi = \pm\sqrt{\frac{r^3 N'(r)}{N(r) - rN'(r)}}, \tag{E.3}$$

with associated energy,

$$E \equiv u_t = -\sqrt{\frac{N^3}{N(r) - rN'(r)}}. \tag{E.4}$$

From these, the angular velocity as measured by a distant observer is,

$$\Omega = \frac{u^\phi}{u^t} = -\frac{N^2(r)}{r^2}\frac{L}{E} = \pm\sqrt{\frac{N(r)N'(r)}{r}}. \tag{E.5}$$

The stability of these circular orbits is determined by the response to perturbations (again similar to the analysis of photon orbits in Appendix B),

$$\dot{\delta r}^2 = -\omega^2 \delta r^2 \tag{E.6}$$

where

$$\omega^2 = \frac{N(r)}{B^2(r)} \left[N''(r) \left(1 + \frac{L^2}{r^2} \right) + \frac{3N^3(r)}{r^4} \frac{L^2}{E^2} \right] \delta r^2. \tag{E.7}$$

When $\omega^2 > 0$, the perturbation is oscillatory and the orbits are stable; when $\omega^2 < 0$ the perturbation grows exponentially. Note that at r_γ, $L^2 \to \infty$ and $\omega^2 < 0$ if $N''(r_\gamma) < 0$, i.e., if any photon rings are observed then timelike geodesics are also unstable at the photon orbit.

Transitions from stable to unstable circular orbits occur when $\omega^2 = 0$. The radius of the innermost stable circular orbit is the minimum $r_{\rm I}$ for which

$$r_{\rm I} = -\frac{3N(r_{\rm I})N'(r_{\rm I})}{3N'^2(r_{\rm I}) - N(r_{\rm I})N''(r_{\rm I})}, \tag{E.8}$$

which is an analogous condition to that for r_γ in Equation 2.7. However, in the absence of knowledge about the particular form of $N(r)$ away from r_γ, it is difficult to place any further general conditions on $r_{\rm I}$ relative to r_γ.

Appendix F

Slowly Rotating Space times

When viewed from the polar axis, approximately appropriate for M87*, by symmetry all axisymmetric space times must produce circular shadows. While limiting ourselves to this viewing angle reduces the impact of space time properties, it does simplify the relationship between the shadow size and the underlying space time geometry.

$$\begin{aligned} ds^2 = &- N(r)^2 \left[1 + a^2 f_t(r, \cos\theta; a^2)\right] dt^2 \\ &+ \frac{B(r)^2}{N(r)^2} \left[1 + a^2 f_r(r, \cos\theta; a^2)\right] dr^2 \\ &+ r^2 \left[1 + a^2 f_\theta(r, \cos\theta; a^2)\right] d\theta^2 \\ &+ r^2 \sin^2\theta \left[1 + a^2 f_\phi(r, \cos\theta; a^2)\right] d\phi^2 \\ &+ 2ag(r, \cos\theta; a^2) dt d\phi, \end{aligned} \tag{F.1}$$

for some set of functions $f_t(r, \cos\theta; a^2)$, $f_r(r, \cos\theta; a^2)$, $f_\theta(r, \cos\theta; a^2)$, $f_\phi(r, \cos\theta; a^2)$, and $g(r, \cos\theta; a^2)$, where we have explicitly enforced the reduction to spherical symmetry when $a = 0$ and reflection symmetry across the equatorial plane.

Because of this latter symmetry, shadow sizes observed by polar viewers must be independent of the sign of the spin. Expanding the above confirms that the lowest-order spin correction enters at a^2 . As a consequence, up to corrections of a^2, the shadow size is that given in Equation 2.10.

F.1 The Polar Photon Sphere

We begin with Equation 3.12 for $\dot{r}^2$,

$$\dot{r}^2 = \frac{r^2}{\tilde{\Sigma}^2}\frac{e^2}{B^2(r)}\left[1 - \frac{q^2+a^2}{r^2}N^2(r)\right]. \tag{3.12}$$

To obtain an equation for $\ddot{r}$, we differentiate with respect to the affine parameterization of nearby geodesics (λ) and take the limit as $\dot{r} \to 0$. That is,

$$\begin{aligned}
\ddot{r} &= \frac{1}{2\dot{r}}\frac{d\dot{r}^2}{d\lambda} \\
&= \frac{1}{2\dot{r}}\left(\frac{\partial \dot{r}^2}{\partial r}\dot{r} + \frac{\partial \dot{r}^2}{\partial \theta}\dot{\theta}\right) \\
&= \frac{1}{2}\left[\frac{r^2}{\tilde{\Sigma}^2}\frac{e^2}{B^2(r)}\right]'\left[1 - \frac{q^2+a^2}{r^2}N^2(r)\right] \\
&\quad - \frac{r^2}{\tilde{\Sigma}^2}\frac{e^2}{B^2(r)}\left[\frac{q^2+a^2}{r^2}N^2(r)\right]' \\
&\quad - \frac{\sin(2\theta)}{\tilde{\Sigma}}\dot{r}\dot{\theta}.
\end{aligned} \tag{F.2}$$

Taking the limit as $r \to r_\gamma$, and therefore $\dot{r} \to 0$ and $r^2 \to (q^2+a^2)N^2(r)$, the first and third terms vanish identically. This leaves

$$\ddot{r} = -\frac{r^2}{\tilde{\Sigma}^2}\frac{e^2}{B^2(r)}\left[\frac{q^2+a^2}{r^2}N^2(r)\right]' \tag{F.3}$$

which we assume vanishes only when the second term does, i.e., $[(q^2+a^2)N^2(r)/r^2]' = 0$. Thus, we have two simultaneous equations for r and q, which combine to give the desired expression, $r_\gamma N'(r_\gamma) = N(r_\gamma)$.

Appendix G

ADM Mass and Spin

The parameters M and a correspond to the ADM mass and spin, respectively, when $N(r)$, $B(r)$, $F(r)$, and $f(r)$ approach their Kerr values at large r. That is, should it be desirable to interpret M and a as the ADM mass and spin, this imposes the following asymptotic conditions on the otherwise unrestricted functions,

$$\begin{aligned} \lim_{r\to\infty} f(r) &= 0 \\ \lim_{r\to\infty} r[N(r) - (1 - M/r)] &= 0 \\ \lim_{r\to\infty} r[B(r) - 1] &= 0 \\ \lim_{r\to\infty} r[F(r) - 1] &= 0. \end{aligned} \tag{G.1}$$

Appendix H

Metric Components

The components of the metric in Equation 3.6 may be written as

$$\begin{aligned} g_{tt} &= -\tilde{\Sigma}\frac{N^2 - a^2F^2\sin^2\theta}{[r - a^2F\sin^2\theta]^2} \\ g_{rr} &= \tilde{\Sigma}\frac{B^2}{N^2} \\ g_{\theta\theta} &= \tilde{\Sigma} \\ g_{\phi\phi} &= \tilde{\Sigma}\sin^2\theta\frac{[r^2 - a^2N^2\sin^2\theta]}{[r - a^2F\sin^2\theta]^2} \\ g_{t\phi} &= \tilde{\Sigma}a\sin^2\theta\frac{[N^2 - rF]}{[r - a^2F\sin^2\theta]^2}. \end{aligned} \tag{H.1}$$

From these we have

$$g_{t\phi}^2 - g_{tt}g_{\phi\phi} = \frac{\tilde{\Sigma}^2N^2\sin^2\theta}{[r - a^2F\sin^2\theta]^2}, \tag{H.2}$$

and therefore, the metric determinant is

$$\sqrt{-g} = \frac{\tilde{\Sigma}^2B}{r - a^2F\sin^2\theta}. \tag{H.3}$$

With the identifications,

$$\begin{aligned} A_1^2(r) &= \frac{r^2\Delta}{N^2(r)(r^2+a^2)^2} \\ A_2^2(r) &= \frac{F^2(r)\Delta}{N^2(r)} \\ A_5(r) &= \frac{N^2(r)}{\Delta B^2(r)}, \end{aligned} \tag{H.4}$$

and $f(r)$ is unchanged, these match Equation 51 of [60] exactly.

Appendix I

Describing Alternative Spherical Spacetimes

Our approach here involves two complementary methods. Firstly, we will provide a brief introduction to metric expansions that are not dependent on any underlying physical theory. These expansions have been designed in such a way that they reduce to the Schwarzschild metric when deviation parameters are set to zero. Despite not being derived from any specific modified theory of gravity, these metrics enable us to explore a wide range of possibilities and can later be mapped to parameters of a fundamental theory for further analysis and also help us quantifying the deviations from GR.

I.1 Metric Expansions

In Table I.1, we review certain metric expansions and focusing on the metric's g_{tt} component since as we demonstrated before in (A.15), shadow size is directly related to radial component of g_{tt} at the photon orbit. Furthermore, we will explain more about these expansions in subsection 2.2.2 .

I.2 Alternative Spacetime

In Table I.2 we review some explicit alternatives to General Relativity. Alternative metrics differ in an important conceptual way from the metric expansions, the correlations are a

Metric	g_{tt}
PN([76, 41],)	$-(1-\frac{2M}{r}+2(\frac{\kappa_1}{r^2}-\frac{\kappa_2}{r^3}+\frac{\kappa_3}{r^4}-\frac{\kappa_4}{r^5}\dots))$
MGBK metric Expansion[83]	$-\left(1-\frac{2M}{r}\right)\left[1-\sum_{n=2}^{\infty}\frac{\gamma_{1,n}M^n}{r^n}-2\left(1-\frac{2M}{r}\right)\sum_{n=2}^{\infty}\frac{\gamma_{4,n}M^n}{r^n}\right]$
RZ metric Expansion [79]	$-\left(1-\frac{r_0}{r}\right)\left[1-\epsilon\frac{r_0}{r}+(a_0-\epsilon)\frac{r_0^2}{r}^2+a_1\frac{r_0^3}{r^3}\right].$
JP metric Expansion[60]	$-\left(1-\frac{2M}{r}\right)\left(1+\sum_{n=2}^{\infty}\frac{\alpha_{1n}M^n}{r^n}\right)^{-2}$

Table I.1: Metric Expansions

consequence of the physical prior that the metric of interest applies and is not an arbitrary truncation of an otherwise infinite series of terms. In this sense, the possible observational constraints are meaningful within the narrow context of the alternative metric.

Similar to previous section, we focus mostly on the g_{tt} component of each of these metrics since in the following chapters we can deduce the shadow size associated with each of these just by using this component of the metric (for simplicity here we redefine r to $\frac{r}{M}$ to have a dimensionless parameter). However, it is worth mentioning that all other components of these metrics are same as the Schwarzschild spacetime unless otherwise stated.

Metric	g_{tt}	g_{rr}
RN(Reissner–Nordström) metric[77]	$-\left(1-\frac{2}{r}+\frac{q^2}{r^2}\right)$	$1/f(r)$
E-ae 1 metric[10]	$-\left(1-\frac{2}{r}+\frac{3^3 c_{13}}{2^4(1-c_{13})\frac{1}{r^4}}\right)$	$1/f(r)$
E-ae 2 metric[10]	$-\left(1-\frac{2-c_{14}}{r}+\frac{(2c_{13}-c_{14})(2-c_{14})^2}{8(1-c_{13})}\frac{1}{r^2}\right)$	$1/f(r)$
Bardeen metric[7]	$-\left(1-\frac{2r^2}{(r^2+q_m^2)^{3/2}}\right)$	$1/f(r)$
Hayward metric [53]	$-\left(1-\frac{2r^2}{r^2+2l^2}\right)$	$1/f(r)$
Birnokov metric[17]	$-\left(1-\frac{2}{r}\left(1-\tanh(\frac{q_m^2}{2r})\right)\right)$	$1/f(r)$
EEH metric[88]	$-\left(1-\frac{2}{r}+\frac{q_m^2}{r^2}-\alpha\frac{2q_m^4}{5r^6}\right)$	$1/f(r)$
Frolov metric[44]	$-\left(1-\frac{(2r-\tilde{q}^2)r^2}{r^4+(2r+\tilde{q}^2)\tilde{l}^2}\right)$	$1/f(r)$
KS metric[63]	$-\left(-\frac{2}{r}+\frac{\sqrt{r^2-\tilde{a}^2}}{r}\right)$	$1/f(r)$
CFM-A and CFM-B metric[19]	$-\left(1-\frac{2}{r}\right)$	$(1-\frac{3}{2r})(1-\frac{4\beta-1}{2r})^{-1}(1-\frac{2}{r})^{-1}$
EMd [46, 47]	$-\left(1-\frac{\sqrt{4r^2+\tilde{q}^4}-\tilde{q}^2}{r^2}\right)$	$\frac{4r^2}{4r^2+\tilde{q}^4}\left(1-\frac{\sqrt{4r^2+\tilde{q}^4}-\tilde{q}^2}{r^2}\right)^{-1}$

Table I.2: Spherically symmetric alternative theories of gravity

In this table we listed some alternative theories of gravity that had been mentioned in [65] and describe a spherically symmetric spacetime around a massive object. $f(r)$ is equal to $1-2M/r$. Additionally, it is worth mentioning that the difference between CFM-A and B relies on β's range, which for CFM-A is $\beta<1$ and for CFM-B is $1<\beta<5/4$

Appendix J

Describing Alternative Axi-symmetric Spacetimes

The metric in Equation 3.6 is sufficiently general to describe a wide range of spinning black hole space times. Here we explicitly demonstrate that it can express a number of specific alternative space times by constructing the associated free functions.

J.0.1 Kerr

We begin with the Kerr metric, written in Boyer-Lindquist coordinates,

$$ds^2 = -\frac{\Delta}{\Sigma}(dt - a\sin^2\theta d\phi)^2 + \frac{\sin^2\theta}{\Sigma}\left[adt - (r^2+a^2)d\phi\right]^2 + \frac{\Sigma}{\Delta}dr^2 + \Sigma d\theta^2, \quad \text{(J.1)}$$

Metric	$N^2(r)/F^2(r)$	$B^2(r)/F^2(r)$	$F(r)$	$f(r)$	$A_1^2(r)$	$A_2^2(r)$	$A_5(r)$
Kerr	Δ	r^2	$r/(r^2+a^2)$	0	1	1	1
Kerr-Newman	$\Delta_{\rm KN}$	r^2	$r/(r^2+a^2)$	0	$\Delta/\Delta_{\rm KN}$	$\Delta/\Delta_{\rm KN}$	$\Delta_{\rm KN}/\Delta$
Hayward	$\Delta_{\rm H}$	r^2	$r/(r^2+a^2)$	0	$\Delta/\Delta_{\rm H}$	$\Delta/\Delta_{\rm H}$	$\Delta_{\rm H}/\Delta$
Bardeen	$\Delta_{\rm B}$	r^2	$r/(r^2+a^2)$	0	$\Delta/\Delta_{\rm B}$	$\Delta/\Delta_{\rm B}$	$\Delta_{\rm B}/\Delta$
Kerr-Sen	$\Delta_{\rm S}$	r^2	$r/[r(r+r_{\rm S})+a^2]$	$rr_{\rm S}$	$\frac{\Delta[r(r+r_{\rm S})+a^2]}{\Delta_{\rm S}(r^2+a^2)}$	$\Delta/\Delta_{\rm S}$	$\Delta_{\rm S}/\Delta$
Baines-Visser	$\Delta_{BV}e^{-2\Phi}$	$r^2e^{-2\Phi}$	r/Ξ^2	$\Xi-(r^2+a^2)$	$\frac{\Xi^2\Delta e^{2\Phi}}{(r^2+a^2)^2\Delta_{BV}}$	$\Delta e^{2\Phi}/\Delta_{\rm BV}$	$\Delta_{\rm BV}/\Delta$

Table J.1: Alternative Axi-symmetric spacetimes
Describing alternative spacetime metrics with Equation 3.6 and the [60] metric.

where $\Sigma = r^2 + a^2 \cos^2\theta$. This form may be immediately represent in the form of Equation 3.6 with appropriate choices for $N(r)$, $F(r)$, $B(r)$, and $f(r)$. Before explicitly stating these (see also Table J.1), we begin with define a function that will appear repeatedly, $u(r) \equiv r/(r^2 + a^2)$, and note that when $F(r) = u(r)$,

$$r - Fa^2 \sin^2\theta = \Sigma u(r), \tag{J.2}$$

i.e., with an appropriate definition of $F(r)$ some of the denominators in Equation 3.6 (or Equation H.1) simplify in such a way that the dependence on the polar angle may be subsumed into factors of Σ. Therefore, inserting this expression for $F(r)$ into Equation 3.6 produces

$$ds^2 = -\frac{\tilde{\Sigma} N^2}{\Sigma^2 u^2(r)}(dt - a\sin^2\theta d\phi)^2 + \frac{\tilde{\Sigma}\sin^2\theta}{\Sigma^2}\left[adt - (r^2 + a^2)d\phi\right]^2 + \tilde{\Sigma}\frac{B^2}{N^2}dr^2 + \tilde{\Sigma}d\theta^2. \tag{J.3}$$

The remaining functions in Equation 3.6 are set by matching the coefficients in Equation 3.6 and Equation J.1. We begin with setting the coefficient of $d\theta^2$, which requires $f(r) = 0$ and thus $\tilde{\Sigma} = \Sigma$. This choice also results the matching of the coefficient in the second term. The first term may be used to set $N(r)$,

$$N^2(r) = \Delta u^2(r), \tag{J.4}$$

and the third sets $B(r)$,

$$B^2(r) = \frac{N^2(r)}{\Delta} = 1. \tag{J.5}$$

These are summarized in Table J.1.

J.0.2 Kerr-Newman

Charged spinning black holes are described in general relativity by the Kerr-Newman metric,

$$ds^2 = -\frac{\Delta_{\rm KN}}{\Sigma}(dt - a\sin^2\theta d\phi)^2 + \frac{\sin^2\theta}{\Sigma}\left[adt - (r^2 + a^2)d\phi\right]^2 + \frac{\Sigma}{\Delta_{\rm KN}}dr^2 + \Sigma d\theta^2, \tag{J.6}$$

which differs from Kerr by the introduction of $\Delta_{\rm KN}$,

$$\Delta_{\rm KN} \equiv r^2 - 2Mr + a^2 + r_Q^2, \tag{J.7}$$

where $r_Q^2 \equiv GQ^2/4\pi\epsilon_0 c^4$ is the black hole charge in gravitational units (CITE). Again, we set $F(r) = u(r)$, which puts the metric in the form of Equation J.3. Then, we adopt

$$\begin{aligned} N^2(r) &= \Delta_{\rm KN} u^2(r) \\ B^2(r) &= \frac{\Delta_{\rm KN}}{\Delta} \\ f(r) &= 0, \end{aligned} \tag{J.8}$$

for which Equation J.3 becomes identical to Equation J.6.

J.0.3 Rotating Hayward

The Hayward metric is originally spherically symmetric, and thus a substitute for Schwarzschild [53]. A rotating analog has been constructed via a procedure analogous to the Newman-Janis algorithm, resulting in a Kerr-like metric with mass replaced by a function of radius (Abdujabbarov et al. 2016, though see Bambi and Modesto, 2013). Expressed in Boyer-Lindquist coordinates, this takes the form

$$ds^2 = -\frac{\Delta_{\rm H}}{\Sigma}(dt - a\sin^2\theta d\phi)^2 + \frac{\sin^2\theta}{\Sigma}\left[adt - (r^2+a^2)d\phi\right]^2 + \frac{\Sigma}{\Delta_{\rm H}}dr^2 + \Sigma d\theta^2, \tag{J.9}$$

where

$$\Delta_{\rm H} = r^2 + a^2 - 2\frac{Mr^4}{r^3 + g^3} \tag{J.10}$$

is modified to eliminate the space time singularity. Like the Kerr-Newman metric, the modification to Kerr is confined to a redefinition of Δ, and thus upon choosing $N^2(r)$, $B^2(r)$, $F(r)$ and $f(r)$, Equation 3.6 reproduces the desired metric.

J.0.4 Rotating Bardeen

The rotating Bardeen metric is nearly identical to the rotating Hayward metric, with the exception that Δ_H is replaced with

$$\Delta_{\rm B} = r^2 + a^2 - 2\frac{Mr^4}{(r^2 + g_*^2)^{3/2}}, \tag{J.11}$$

J.0.5 Kerr-Sen

The Kerr-Sen metric describes a charged black hole that arises in a heterotic string theory. It is characterized by an additional charge, related to a length scale via $r_{\rm S} = Q^2/4\pi\epsilon_0 Mc^2$ (Sen 1992). In Boyer-Lindquist coordinates, this metric may be written as,

$$ds^2 = -\left(1 - \frac{2Mr}{\Sigma_{\rm S}}\right)dt^2 - \frac{4Mra\sin^2\theta}{\Sigma_{\rm S}}dtd\phi + \left[r(r+r_{\rm S}) + a^2 + \frac{2Mra^2\sin^2\theta}{\Sigma_{\rm S}}\right]\sin^2\theta d\phi^2 + \frac{\Sigma_{\rm S}}{\Delta_{\rm S}}dr^2 + \Sigma_{\rm S}d\theta^2 \tag{J.1}$$

where

$$\Sigma_{\rm S} \equiv r(r+r_{\rm S}) + a^2\cos^2\theta\Delta_{\rm S} \quad \equiv r(r+r_{\rm S}) - 2Mra^2, \tag{J.13}$$

(Narang et al. 2020 [arXiv:2002.12786]). Comparing the metric coefficients with those in Equation 3.6, it is immediately clear from the coefficient of $d\theta^2$ that $f(r) = rr_{\rm S}$. Setting the remaining free functions,

$$\begin{aligned} F(r) &= r/[r(r+r_{\rm S}) + a^2] \\ N^2(r) &= \Delta_{\rm S}F^2(r) \\ B^2(r) &= F^2(r), \end{aligned} \tag{J.14}$$

brings Equation 3.6 into agreement with Equation J.12.

J.0.6 Baines-Visser Metric

In arXiv:2303.07380 a family of metrics describing axisymmetric space times is proposed that admits separable Hamilton-Jacobi and Klein-Gordon equations,

$$\begin{aligned} ds^2 = &-\frac{\Delta_{\rm BV}e^{-2\Phi} - a^2\sin^2\theta}{\Xi^2 + a^2\cos^2\theta}dt^2 - 2\frac{a\left(\Xi^2 - \Delta_{\rm BV}e^{-2\Phi} + a^2\right)\sin^2\theta}{\Xi^2 + a^2\cos^2\theta}dtd\phi \\ &+ \frac{\left[\left(\Xi^2 + a^2\right)^2 - e^{-2\Phi}\Delta_{\rm BV}a^2\sin^2\theta\right]\sin^2\theta}{\Xi^2 + a^2\cos^2\theta}d\phi^2 + \frac{\Xi + a^2\cos^2\theta}{\Delta_{\rm BV}}dr^2 + \left(\Xi^2 + a^2\cos^2\theta\right)d\theta^2, \end{aligned} \tag{J.15}$$

where $\Phi(r)$, $\Delta_{\rm BV}(r)$, and $\Phi(r)$ are three free functions of radius. Thus, this family metric is suggested as a useful class of foils for general relativity. It is a special case of Equation 3.6,

with

$$
\begin{aligned}
f(r) &= \Xi(r) - (r^2 + a^2) \\
F(r) &= \frac{r}{\Xi(r)} \\
N^2(r) &= \frac{r^2 \Delta_{\mathrm{BV}}(r) e^{-2\Phi(r)}}{\Xi^2(r)} \\
B^2(r) &= \frac{r^2 e^{-2\Phi(r)}}{\Xi^2(r)}.
\end{aligned}
\tag{J.16}
$$